Comparative Study of Five Outcrop Chalks Flooded at Reservoir Conditions: Chemo-Mechanical Behaviour and Profiles of…

Article *in* Transport in Porous Media · September 2017

DOI: 10.1007/s11242-017-0953-6

9 authors, including:

Pål Østebø Andersen
University of Stavanger (UiS)
31 PUBLICATIONS **68** CITATIONS
SEE PROFILE

Wenxia Wang
University of Stavanger (UiS)
3 PUBLICATIONS **4** CITATIONS
SEE PROFILE

M.V. Madland
University of Stavanger (UiS)
73 PUBLICATIONS **719** CITATIONS
SEE PROFILE

S. R. Bertolino
National Scientific and Technical Research C…
32 PUBLICATIONS **123** CITATIONS
SEE PROFILE

Comparative Study of Five Outcrop Chalks Flooded at Reservoir Conditions: Chemo–Mechanical Behaviour and Profiles of Compositional Alteration

P. Ø. Andersen[1, 2, *] · W. Wang[1, 2] · M. V. Madland[1, 2] · U. Zimmermann[1, 2] · R. I. Korsnes[1, 2] · S. R. A. Bertolino[3] · M. Minde[1, 2, 4] · B. Schulz[5] · S. Gilbricht[5]

1 Department of Petroleum Technology, University of Stavanger, Stavanger, Norway

2 The National IOR Centre of Norway, University of Stavanger, Ullandhaug, 4036 Stavanger, Norway

3 FaMAF, Universidad Nacional de Córdoba, Medina Allende s/n, Ciudad Universitaria, Córdoba, Argentina.

4 IRIS AS, International Research Institute of Stavanger, Ullandhaug, 4036 Stavanger, Norway

5 TU Bergakademie Freiberg, Department of Economic Geology and Petrology, Freiberg/Saxony, Germany

* Corresponding author:

P. Ø. Andersen (pal.andersen@uis.no)

Abstract

This study presents experimental results from a flooding test series performed at reservoir conditions for five high porosity Cretaceous on–shore chalks from Denmark, Belgium and the USA, analogous to North Sea reservoir chalk. The chalks are studied in regard of their chemo–mechanical behavior when performing tri–axial compaction tests while injecting brines (0.219 mol/L $MgCl_2$ or 0.657 mol/L NaCl) at reservoir conditions for 2 – 3 months (T = 130 °C; 1 PV/d). Each chalk type was examined in terms of its mineralogical and chemical composition before and after the mechanical flooding tests, using an extensive set of analysis methods, to evaluate the chalk– and brine–dependent chemical alterations. All $MgCl_2$ flooded cores showed precipitation of Mg–bearing minerals (mainly magnesite). The distribution of newly formed Mg–bearing minerals appears to be chalk–dependent with varying peaks of enrichment. The chalk samples from Aalborg originally contained abundant opal–CT, which was dissolved with both NaCl and $MgCl_2$ and partly re–precipitated as Si–Mg–bearing minerals. The Aalborg core injected with $MgCl_2$ indicated strongly increased specific surface area (from 4.9 m^2/g to within 7 – 9 m^2/g). Mineral precipitation effects were negligible in chalk samples flooded with NaCl compared to $MgCl_2$. Silicates were the main mineralogical impurity in the studied chalk samples (0.3 – 6 weight %). The cores with higher SiO_2 content showed less deformation when injecting NaCl–brine, but more compaction when injecting $MgCl_2$–brine. The observations

were successfully interpreted by mathematical geochemical modelling which suggests that the re–precipitation of Si–bearing minerals leads to enhanced calcite dissolution and mass loss (as seen experimentally) explaining the high compaction seen in $MgCl_2$ flooded Aalborg chalk.

Our work demonstrates that the original mineralogy, together with the newly formed minerals can control the chemo–mechanical interactions during flooding and should be taken into account when predicting reservoir behaviour from laboratory studies. This study improves the understanding of complex flow–reaction mechanisms also relevant for field scale dynamics seen during brine injection.

Key words Chalk compaction · Creep acceleration · Dissolution–precipitation · Core flooding at reservoir conditions · Non–carbonate composition

List of parameters

a_h	Activity of H^+
A	Area, m^2
C_i	Concentration variable of species i, mol/L pore volume
D	Core diameter, mm
$k_{1,i,}\, k_{2,i,}$	Reaction rate parameter for mineral i, mol/m^2/s
k_o	Original permeability, mD
K_i	Solubility constant of mineral i, –
L	Core length, mm
M	Mass, g
p_i, q_i, r_i, n_i	Reaction order parameters, –
Q	Injection rate, mL/d
V	Volume, L or cm^3
$\delta^{13}C$	A measure of the ratio of stable isotopes ^{13}C and ^{12}C, ‰
$\delta^{18}O$	A measure of the ratio of stable isotopes ^{18}O and ^{16}O, ‰
ε	Axial creep strain, %
P	Solid density, cm^3/L
ρ_w	Brine density, cm^3/L
Φ	Porosity, %
Ω_i	Saturation state of mineral i, –

Subscripts

bulk	Bulk volume (solids and pores)
core	Based on the core piece
dry	Dry sample
end	State after compaction–flooding tests
o	Original / unflooded state
pyc	Based on pycnometry
sat	Saturated sample

Abbreviations

AA	Aalborg
aq	Aqueous
b.d.l.	Below detection limit
BET	Brunauer–Emmett–Teller theory
DI–H_2O	Deionized water
DW	Distilled water
EDS	Energy–dispersive X–ray spectroscopy
EDX	Energy–dispersive X–ray
FEG–SEM	Field emission gun–scanning electron microscopy
FEP	Fluorinated ethylene propylene
Fm	Formation
HPLC	High performance liquid chromatography
ICP–AES	Inductively coupled plasma–atomic emission spectroscopy
ICP–MS	Inductively coupled plasma–mass spectrometry
ICS	Ion chromatography system
KA	Kansas
LI	Liège
LOI	Loss on ignition, wt%
LVDT	Linear variable displacement transducer
MLA	(Automated SEM) mineral liberation analysis
MO	Mons
PID	Proportional integral derivative
PPM	Part per million
PV	Pore volume
s	Solid

SK	Stevns Klint
SMOW	Standard mean ocean water composition in Vienna Pee Dee Belemnite
SSA	Specific surface area, m^2/g
Sup. Mat.	Supplementary material
TDS	Total dissolved solids, g/L
TEM	Transmission electron microscopy
TOT/C	Total carbon, wt%
wt%	Weight percent
XRD	X–ray diffraction

1 Introduction

The physicochemical interplay between minerals and fluids is of great importance in many natural and industrial settings (Putnis 2002; Ruiz–Agudo et al. 2014). Water injection into reservoirs is extensively applied to increase oil recovery and the inherent chemical fluid–rock interactions and subsequent changes of mechanical properties have led to investigations towards more optimal injection fluids. In the chalk field Ekofisk in the North Sea, reservoir compaction (initiated by production) continued even after reservoir re–pressurization by seawater injection. The relationships between mechanical properties of reservoir chalk and pore fluids have been of significant interest in scientific research and industry ever since (Hermansen et al. 1997, 2000; Risnes and Flaageng 1999; Nagel 2001; Risnes et al. 2005; Fabricius and Borre 2007).

Research shows that compaction is affected mechanically by effective stresses, but also depends on porosity, chemistry, diagenetic processes and cementation (Engstrøm 1992; Havmøller and Foged 1996; Bjørlykke and Høeg 1997; Zhang et al. 2010; Bjørlykke 2014). Varying the ionic concentrations of Ca^{2+}, Mg^{2+} and SO_4^{2-} in the injected brines can lead to changes (weakening) in mechanical properties of chalk rock (Newman 1983; Strand et al. 2003; Korsnes et al. 2006a, 2006b, 2008; Madland et al. 2008). This effect has amongst others been related to chemical reactions involving dissolution of the chalk matrix (Madland et al. 2011; Zimmermann et al. 2013, 2015; Megawati et al. 2015; Wang et al. 2016), which is also coupled to formation of new minerals. Injection of synthetic seawater into Liège chalk resulted in precipitation of anhydrite and Mg–bearing minerals, while abundant Mg–bearing minerals formed when $MgCl_2$ was injected (Madland et al. 2011). Long–term $MgCl_2$–flooding tests (516 and 1072 d) on Liège chalk produced significant mineralogical changes where complete sections of the core were

transformed from calcite to Mg–bearing minerals (Nermoen et al. 2015; Zimmermann et al. 2015), which is in line with modelling results (Hiorth et al. 2013). Magnesite was the dominant new phase. Compaction while exposing the rock to inert brines normally results in less deformation compared to using reactive brines that can dissolve more calcite (Hellmann et al. 2002). Switching injection brine from 0.219 mol/L $MgCl_2$ to a similar brine that was equilibrated with chalk, and thus inert, significantly reduced the creep rate (Megawati et al. 2011). Several researchers have also emphasized the role of non–carbonate minerals in chalk (Fabricius 2001; Fabricius et al. 2007; Hjuler 2007; Strand et al. 2007; Hjuler and Fabricius 2009; Megawati et al. 2011). Fabricius and Borre (2007) suggest that formation of Ca–Si complexes can lead to increased solubility of calcite with possible impacts on geological processes in the North Sea. Madland et al. (2011) tested Liège cores while flooding 0.1095 mol/L $MgCl_2$ for ~ 17 d. Parts of the original non–carbonate phase, in form of silicate minerals, were dissolved and re–precipitated forming a new silicate mineral phase with a clay–like appearance as observed in Scanning Electron Microscopy (SEM) images. Megawati et al. (2015) studied a variety of outcrop chalks in terms of their compaction behaviour and noted a strong dependence on non–carbonate content. In particular, clean chalks displayed a very slow creep phase with a sudden acceleration later on, while more impure chalks had a high and steady compaction. Research has also shown that compaction can affect chemistry by pressure solution (Newman 1983): when increasing the applied stress on a core, which is transferred to the grain-to-grain contacts, these contact points effectively obtain increased mineral equilibrium constants compared to open surfaces (Paterson 1973; Rutter 1976) which can result in a progressive local dissolution (Hellmann et al. 2002; Zhang et al. 2011). Neveux et al. (2014) observed increased brine-mineral interaction during flooding experiments when systematically increasing the differential stresses.

Outcrop chalks and synthetic brines are ideally suited for systematic research. Searching for reservoir chalk substitutes, it is desirable to have similarity in mineralogy, sedimentary age and environment, permeability and porosity, hence combining geological with engineering data sets. In this contribution we test samples from five outcrop chalks of Cretaceous age from Kansas, Mons, Liège, Aalborg and Stevns Klint. They have similar age (Cretaceous) and porosity as North Sea reservoir chalk. The Mons and Stevns Klint samples were pure (> 99 wt% calcite), while the others contained more impurities. Previous XRD analyses of the clay fraction (<2μm) from the five chalk types has shown significant differences in mineralogical assemblage (Bertolino et al. 2013), indicative of different diagenetic conditions. Stevns Klint and Aalborg

chalks have been suggested as suitable geomechanical analogues to the Valhall field chalk due to their modest calcite redistribution and poorly connected particles (Hjuler and Fabricius 2009). Liège chalk is comparable to the Ekofisk field in terms of mechanical properties (Collin et al. 2002; Jarvis 2006; Hjuler and Fabricius 2009). The aim in this work is to investigate how different chalks behave under similar experimental conditions. In similarity to the work by Megawati et al. (2015), chalk cores from the mentioned five outcrops were flooded with two simplified brines (0.219 mol/L $MgCl_2$ or 0.657 mol/L NaCl) at Ekofisk reservoir temperature, 130 °C, while compacting in creep state. Strain and effluent measurements were taken continuously. The tests in this work were performed for a longer period of time (2 – 4 months) to properly document the creep behavior for the various outcrops. The main new contribution of this paper is, however, the comparative analysis of chemical alterations along the cores after the compaction–flooding tests: each core was divided along its flooding direction into 7 slices of comparable size (see Fig. 1b, in 2.2.1). Further, each slice was examined in terms of composition and mineralogy using geological analysis tools such as pycnometry, field emission gun scanning electron microscopy (FEG–SEM), mineral liberation analyses (MLA), X–ray diffraction (XRD), C–O stable isotope analyses, whole–rock geochemistry and measurement of specific surface area (Brunauer–Emmett–Teller (BET) method with liquid nitrogen). This allows a qualitative and quantitative description of the alteration profiles along each core. The measurements were compared to representative unflooded material. Cutting a core to examine individual slices has been performed previously in works such as Megawati et al. (2015); Nermoen et al. (2015); Zimmermann et al. (2015); Wang et al. (2016), but have been limited to the study of one chalk type or one core and using only a few of the methods considered in this paper, making knowledge transfer more restricted. In particular, we compare five different chalk types exposed to similar experimental conditions. This work will focus on the geochemical alterations resulting from the tests. Impacts on engineering properties such as porosity and permeability will be left for future publication. We will highlight possible relations between the chemo–mechanical behavior and the chalk types, which may originate from differences in non–carbonate mineral content, textural differences or geological histories. This can add more understanding to whether and to which extent non–carbonates in chalks play a role in the water–weakening process and allow us to evaluate the feasibility of these on–shore chalks when comparing to reservoir chalks.

2 Experimental procedures and methods

2.1 Core material and injection brines

Outcrop chalks were collected from five locations (from old to young): Kansas (KA), Mons (MO), Liège (LI), Aalborg (AA), and Stevns Klint (SK), see Table 1 for more details. All five types were deposited during the Cretaceous. Mons chalk (from the Trivières Formation) and Stevns Klint chalks are very pure (> 99 weight percent (wt%) calcite), Kansas and Liège chalks are less pure with calcite content around 95 – 97 wt%, and Aalborg chalk contains 92 – 94 wt% calcite.

More details on the mentioned chalks in terms of petrography, petrophysics and mineralogy can be found in Molenaar and Zijlstra (1997); Gaviglio et al. (1999); Fabricius (2001); Frykman (2001); Tang and Firoozabadi (2001); Hart et al. (2004, 2005); Schroeder et al. (2006); Stenstad (2006); Strand et al. (2007); Hjuler and Fabricius (2009); Bertolino et al. (2013). Mechanical properties and compositions will be presented.

Table 1 Geographical origin, geological age and calcite wt% of the studied chalks.

Sample	Abbreviation	Location	Formation/Member	Age	wt% calcite
Kansas	KA	USA, Niobrara	Niobrara Formation, Fort Hays Member	Late Cretaceous	95–97
Mons	MO	Belgium, Harmignies	Trivières Formation	Campanian	>99
Liège	LI	Belgium, Hallembaye	Gulpen Formation	Campanian	95–97
Aalborg	AA	Denmark, Rørdal	Tor Formation, Rørdal Member	Maastrichtian	92–94
Stevns Klint	SK	Denmark, Sigerslev	Tor Formation, Sigerslev Member	Maastrichtian	>99

Table 2 contains information of the core samples applied in the tests. The original solid density (ρ_{o-pyc}) (between 2.67 and 2.70 g/cm^3), estimated by pycnometry measurements (see 2.2.9) of unflooded end pieces (Fig. 1a), is similar to that of calcite mineral, 2.71 g/cm^3, but slightly lower, especially for AA5 (2.67 g/cm^3), AA1 (2.67 g/cm^3) and AA21 (2.67 g/cm^3). A second estimate of solid density was obtained using the whole cores (ρ_{o-core}), from dividing the dry mass by the solid volume:

$$\rho_{o-core} = \frac{M_{dry,o}}{V_{bulk,o} - (M_{sat,o} - M_{dry,o})/\rho_w}, \quad (1)$$

where $M_{dry,o}$ (g) is dry weight, $M_{sat,o}$ (g) saturated weight, $V_{bulk,o}$ (cm^3) bulk volume and ρ_w (g/cm^3) brine density. These measurements yielded a wider range (between 2.63 and 2.71 g/cm^3)

with often lower values (not more than 0.04 g/cm^3 as seen for AA21 and SK1) than the pycnometry estimates, although for KA6 (+0 g/cm^3), KA8 (+0.01 g/cm^3), AA1 (+0 g/cm^3) and SK2 (+0.02 g/cm^3) the estimate was the same or higher. The original porosities (φ_o) were high, in the range 37 – 47 %. The initial permeabilities (k_o) were in the range 1.2 – 3.2 mD.

All cores were flooded for a period of 60 to 95 days (d), besides SK1 (45 d) and AA1 (115 d). For SK1 and AA1 mainly compaction results will be presented in this work, to illustrate repeatability compared to the cores SK6 and AA5. These four tests all applied the same injection brine: $MgCl_2$.

Table 2 Core labels, applied brines, dry core weight $M_{dry,o}$ (g), length L_o (mm), diameter D_o (mm), solid density from pycnometry of end pieces ρ_{o-pyc} (g/cm^3), and of whole core ρ_{o-core} (g/cm^3), porosity φ_o (%), permeability k_o (mD), flooding rate Q (corresponding to 1 pore volume per day, PV/d), flooding time T (d), and specific surface area SSA (m^2/g). Index 'o' refers to 'original state' before flooding and compaction. Results from SK1 and AA1 (marked *) are focused on compaction behaviour in this work.

Core	Brine	$M_{dry,o}$ (g)	L_o (mm)	D_o (mm)	ρ_{o-pyc} (g/cm^3)	ρ_{o-core} (g/cm^3)	φ_o (%)	k_o (mD)	Q (ml/min)	T (d)	SSA (m^2/g)
KA6	NaCl	134.90	69.7	38.1	2.70	2.70	37.0	1.47	0.020	61	
KA8	$MgCl_2$	136.24	70.1	38.1	2.70	2.71	37.0	1.96	0.020	75	
MO12	NaCl	124.52	69.8	38.1	2.70	2.67	41.4	1.58	0.023	61	
MO10	$MgCl_2$	125.58	70.3	38.1	2.70	2.68	41.5	1.19	0.023	60	
LI2	NaCl	126.05	72.7	38.2	2.69	2.67	43.3	1.75	0.025	90	
LI1	$MgCl_2$	112.38	68.9	37.1	2.68	2.66	43.3	1.92	0.022	65	
AA21	NaCl	112.96	70.4	38.2	2.67	2.63	46.7	1.22	0.026	61	
AA5	$MgCl_2$	112.33	70.4	38.1	2.67	2.65	47.2	1.34	0.026	63	
AA1*	$MgCl_2$	119.84	75.0	38.1	2.67	2.67	47.5	1.50	0.028	115	
SK2	NaCl	121.31	73.1	38.0	2.69	2.71	45.9	3.20	0.026	91	
SK6	$MgCl_2$	115.08	70.3	38.1	2.69	2.68	46.4	2.69	0.028	61	
SK1*	$MgCl_2$	117.41	74.0	38.1	2.69	2.65	47.4	2.34	0.028	45	

Two brines were used for core flooding: 0.219 mol/L $MgCl_2$ and 0.657 mol/L NaCl, see Table 3. Their ionic strength is the same as of North Sea seawater: 0.657.

Table 3 Brine compositions in flooding tests. TDS=total dissolved solids.

Brine	Cl^- (mol/L)	Mg^{2+} (mol/L)	Na^+ (mol/L)	Ionic strength	TDS (g/L)
$MgCl_2$	0.438	0.219	0	0.657	20.84
NaCl	0.657	0	0.657	0.657	38.4

2.2 Experimental preparation and procedures

2.2.1 *Flooding experiments at 130 °C in a standard tri–axial cell*

Cylindrical samples were drilled from blocks collected from the five different outcrops (Table 1). Each sample was divided into three parts along the flooding direction (Fig. 1a). The central part was cut to a cylindrical core of diameter ~ 37 and ~ 38 mm and length ~ 70 mm and used for flooding–compaction tests. The two adjacent end pieces were used for analysis of unflooded material (Fig. 1a).

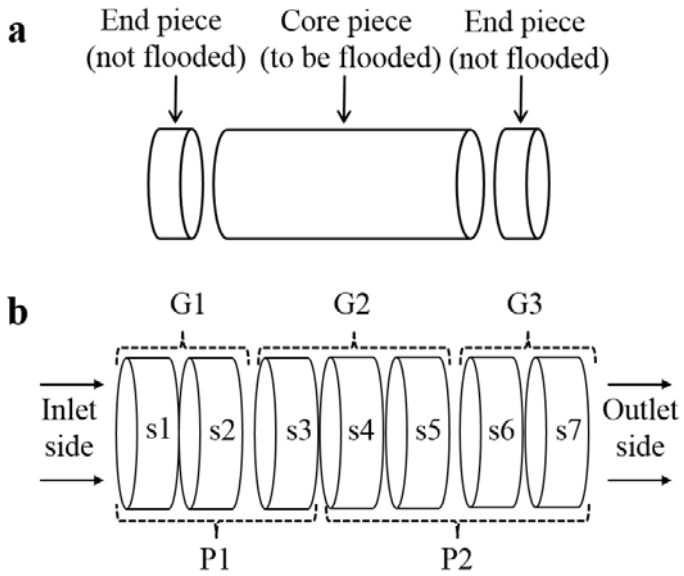

Fig. 1 (a): Material selection procedure: A cylindrical sample is cut into 3 pieces: the central core to be used in flooding–compaction tests and two adjacent end pieces used to measure properties of unflooded material, assumedly also representative of the core. (b): Scheme of the sectioning of the core after the flooding–compaction tests. Arrows indicate flow direction. The core was first cut into two parts P1 and P2 from which solid density was measured by dry weight and solid volume. The core was further cut into slices s1 – s7 (from inlet to outlet) which were grouped into G1 (s1+s2), G2 (s3+s4+s5), and G3 (s6+s7). Each group was measured with pycnometry. The slices were analyzed using the methods described in 2.2.

The cores have a length to diameter ratio close to two so that their strength can be expected to be insensitive to differences in diameter (see e.g. Fig. 7.2 on page 257 in (Fjær et al. 2008)). After preparation, the cores were dried for 12 hours in a heating chamber at 100 °C to remove more than 99 % water in the core before the dry mass $M_{dry,o}$ was determined. The calcite crystals are assumed to be unaffected by the drying conditions. Then the cores were evacuated by vacuum prior to being saturated with distilled water (DW) and then weighed to obtain the saturated mass $M_{sat,o}$. Porosity was then calculated from the ratio of volume water that could be saturated in the dried core divided by the bulk volume $V_{bulk,o}$ of the core:

$$\varphi = \frac{(M_{sat,o} - M_{dry,o})}{\rho_w V_{bulk,o}}. \quad (2)$$

ρ_w is the DW density. Calculated porosity values are listed in Table 2. The same experimental procedure was applied on all the cores studied in this paper such that brine– and chalk–dependent behaviour could be distinguished. The saturated cores were mounted into identical tri–axial cells (for a description of the setup, see Fig. 2). Three Gilson (model 307 High Performance Liquid Chromatography–HPLC) pressure pumps were connected to each tri–axial cell enabling independent control of the piston pressure, confining pressure (radial stress), and injected flow rate (i.e. pump 1 to 3 in Fig. 2). The confining pressure balances the piston such that the axial stress has to be calculated from the confining pressure plus the piston pressure, (see Eqn. 1 in (Nermoen et al. 2015)). A backpressure regulator was placed down–stream of the core to control the pore pressure and at the same time allow for continuous sampling of the effluent fluids. The cells were equipped with a heating jacket and a regulating system (Omron E5CN) with precise PID (Proportional Integral Derivative) temperature control (+/– 0.1 °C). The axial strain was measured by an external axial linear variable displacement transducer (LVDT) placed on top of the piston to monitor the sample length with time. To isolate the core from the confining oil, a heat shrinkage sleeve (1 – ½" Fluorinated Ethylene Propylene (FEP) with diameter of 33 – 43 mm and 0.5 mm wall thickness) was installed between the core and the confining oil. After core mounting, the confining pressure was increased to 0.5 MPa. Thereafter the experiments were conducted according to the following stages:

1. The core samples were flooded with 3 pore volumes (PVs) of distilled water (DW) overnight at ambient temperature to remove any salt precipitates that could affect the flooding tests. This flooding procedure does not significantly alter the geochemical measurements of the non–salt minerals in the core.
2. Change from flooding with DW to $MgCl_2$ or NaCl by attaching the flooding cell into the flow loop (see Fig. 2). The ion compositions of the injected brines are shown in Table 3. Throughout the rest of the test, the flow rate was set to 1 initial PV per day (Table 2).
3. The confining pressure and pore pressure were increased to 1.2 and 0.7 MPa, respectively before the temperature was raised to 130 °C. The pore pressure and temperature were subsequently kept constant throughout the test. The core was left to equilibrate overnight.
4. After equilibration overnight, the confining pressure was increased from 1.2 MPa up to its creep stress by injecting hydraulic oil at a constant flow rate into the confining chamber using pump 2. During pressurization the piston pressure was set to 0.5 MPa to slightly

overcome friction of the piston (0.3 – 0.4 MPa). This increased the axial stress to a value of 0.1 – 0.2 MPa above the radial stress. Because the additional axial stress is small compared to the radial stress the stress condition can be considered near hydrostatic. The stress–strain behaviour was monitored during increase in confining pressure. The bulk modulus parameter was calculated as the ratio of hydrostatic effective stress σ_h divided by volumetric strain ε_V during the linear deformation of the loading phase (see Fig. 6 in 3.7). The radial strain was not monitored and was for simplicity assumed equal to the axial strain ε_a (which is reasonable during hydrostatic deformation):

$$\text{Bulk modulus} = \frac{\sigma_h}{\varepsilon_V} \approx \frac{\sigma_h}{3\varepsilon_a} \quad (3)$$

When the rock began to deform plastically (Fig. 7 in 3.7), i.e. when the stress–strain behaviour became non–linear, the yield point, i.e. the stress at onset of yield, was noted (Table 8). The confining pressure was further increased to the chosen creep stress (up to 8.5 – 23 MPa, Table 8 in 3.7) before the cores where left to compact in the following creep phase (deformation at constant stress).

The axial deformation at constant temperature, stress and pressure conditions (termed creep) was monitored during continuous flooding of $MgCl_2$ or NaCl–brine. The creep magnitude through time is shown in Fig. 7. The pore pressure and confining pressure varied within 0.1 MPa such that the effective stresses were stable throughout the test period (assuming the Biot stress coefficient is ~ 1, see Fjær et al. (2008), p. 33).

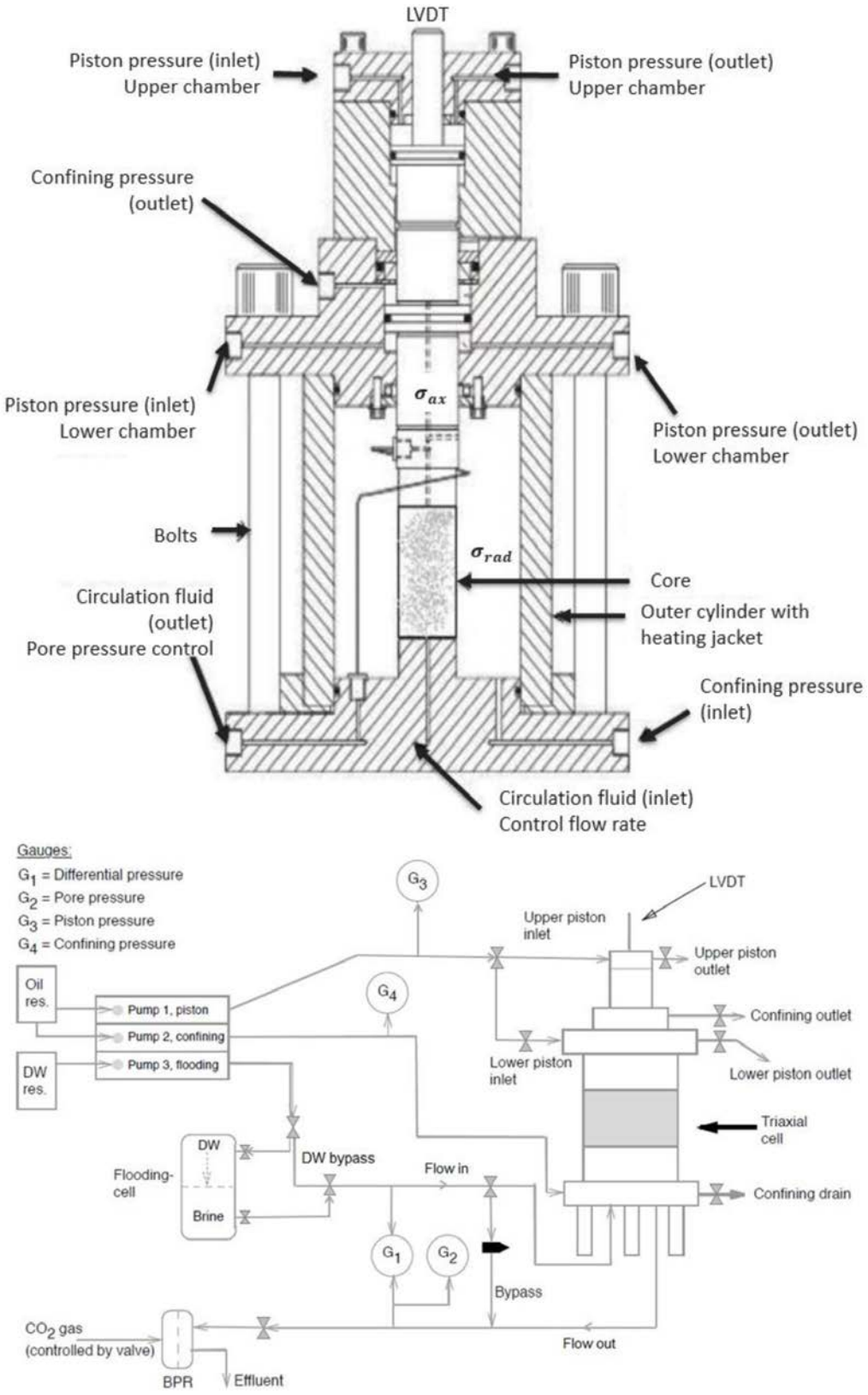

Fig. 2 The experimental setup used in the flooding-compaction tests (figure originally from Nermoen et al. (2016), where more details are presented). Three pumps (piston, confining, and flooding pump) were connected to the tri–axial cell (seen in detail in top figure). The flooding cell contained distilled water (upper chamber) and $MgCl_2$/NaCl (lower chamber). Injection fluid enters the cell at 'Circulation fluid (inlet)' passes through the compacting core and is led out of the cell at 'Circulation fluid

(outlet)'. The whole setup was connected to a computer and complete data, including confining, pore and piston pressure, flooding rate and time were logged automatically.

The pore pressure, hydraulic pressure difference, confining pressure, piston pressure, sample length (axial strain) and flooding time were logged continuously via a LabView program. Before dismantling the core, the sample was cleaned by injecting 3 PVs of distilled water to avoid precipitation of salts from the $MgCl_2$ and NaCl brines during drying. The saturated weight ($M_{sat,end}$) was measured immediately after the dismantling of the cell. Then the core was placed in a drying cabinet at 100 °C and weighed several times until the dry mass ($M_{dry,end}$) stabilized. Each core was first cut into two parts P1 and P2 (see Fig. 1b) from which the solid mass and solid volume (from pycnometry) were used to estimate solid density ($\rho_{end-pyc}$). The core was further cut into seven slices, labelled s1 (inlet) to s7 (outlet), using a Struers Discotom–5 cutting machine (see Fig. 1b for the sectioning scheme). The slices were grouped into G1 (s1+s2), G2 (s3+s4+s5) and G3 (s6+s7) as seen in Fig. 1b and a solid density estimate ($\rho_{end-pyc}$) was made by pycnometry for each group. The slices were then individually subjected to extensive geochemical analysis to identify the mineralogical changes along the core.

In the following we list the analytical techniques used to study the core material prior and post flooding. Details regarding each technique, equipment and settings used and resulting accuracy are elaborated in the Supplementary Material (Sup. Mat.).

2.2.2 *Field Emission Gun–Scanning Electron Microscopy (FEG–SEM)*

Fresh surfaces of unflooded and flooded material were examined to obtain visual images of the grains and rock structure on µm scale.

2.2.3 *X–Ray Diffraction (XRD)*

Provides the mineralogical composition of bulk samples (ca 1 g).

2.2.4 *Automated SEM Mineral liberation analysis (SEM–MLA)*

Applied to thin sections to estimate mineralogical distribution.

2.2.5 *Stable isotope geochemistry (C–O isotopes)*

Oxygen and carbon isotope composition was measured on bulk samples.

2.2.6 *Mass measurements*

Each core was measured before and after flooding to detect mass changes.

2.2.7 *Ion chromatography*

Effluent samples were collected continuously. The concentrations of ions Mg^{2+}, Na^{+}, Cl^{-} and Ca^{2+} were quantified.

2.2.8 *Inductively coupled plasma–atomic emission spectroscopy (ICP–AES)*

Analysis of effluent samples to obtain Si^{4+} concentrations.

2.2.9 *Pycnometry (solid density estimation)*

Solid volume of bulk samples was measured with pycnometer. In combination with dry weight, solid density was be calculated.

2.2.10 *Specific surface area (SSA)*

Specific surface area of bulk samples was measured by the Brunauer–Emmett–Teller (BET) theory.

2.2.11 *Whole–rock geochemistry (geochemical composition)*

Sample bulk material (ca 1 g) from unflooded material or each slice was examined for geochemical composition.

3 Results

3.1 Field Emission Gun–Scanning electron microscopy (FEG–SEM)

3.1.1 *Unflooded samples*

The chalk samples from Kansas are coccolithic mudstone or wackestone, characterized by moderately preserved coccolithophores. Calcite grains often show significant overgrowth and intra–fossil porosity is partly preserved (Fig. 3a, pink arrow, Supplementary Material (Sup. Mat.) Fig. 1a). The microfossils are often filled with calcite crystals. The Mons chalk cores, collected from the Trivières Formation, are pure coccolithic mudstones. Large amounts of very small coccoliths and broken calcite crystals of organic or unknown origin are observed (Sup. Mat. Fig. 1b). Moderately well–preserved coccoliths are abundant. In the coccolithic mudstone from Liège, the microfossils are well–preserved and some overgrowth and recrystallization can be observed. The rocks contain significant amounts of shell fragments, also from macrofossils (Sup. Mat. Fig. 1c). Aalborg chalk cores can be classified as a coccolithic mudstone or wackestone with large numbers of foraminifer shells and even layers of macrofossil debris (Sup. Mat. Fig. 1d). Coccolithophores are well–preserved, but commonly show some overgrowth. Intra–fossil porosity is mostly preserved (Fig. 3b, pink arrow). This chalk contains accumulations of well–developed opal–CT lepispheres that often occur in larger intrafossil pores (Fig. 3b, yellow square). Chalk cores from Stevns Klint consist of extremely pure coccolithic mudstone. Well–preserved coccolithophores and foraminifer shell fragments exist. Larger pore spaces of shell fragments are filled with minute calcite grains (Fig. 3c, pink arrow). Only a limited degree of overgrowth and recrystallization can be observed (Sup. Mat. Fig. 1e).

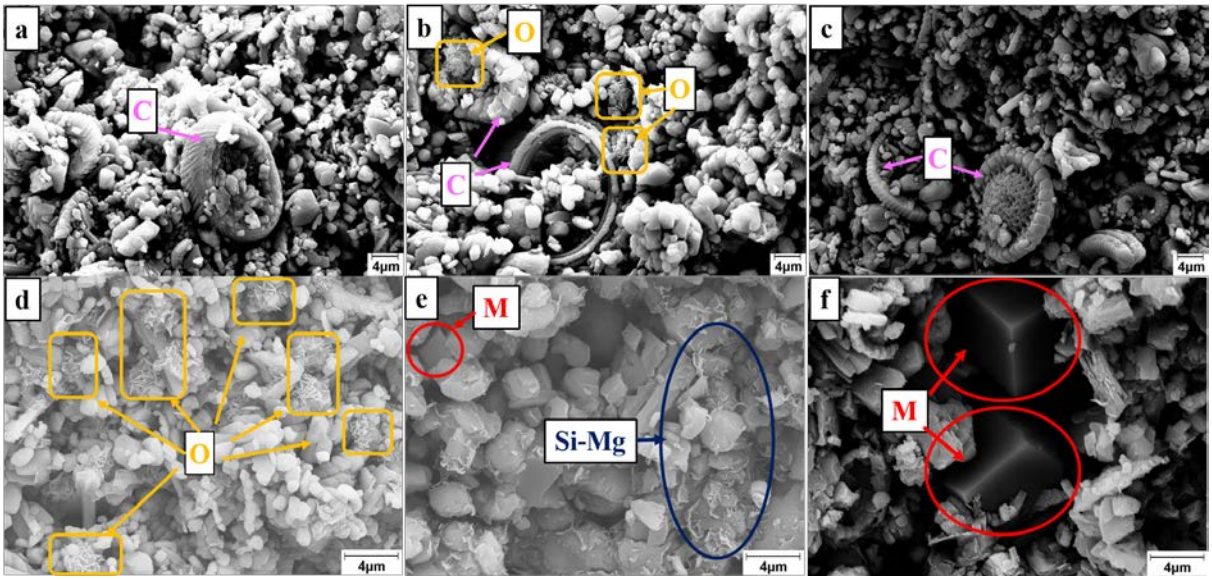

Fig. 3 SEM secondary electron (SE) images of unflooded material (end pieces) and flooded cores, with non–polished sample surfaces. (a): Unflooded Kansas chalk; (b): Unflooded Aalborg chalk; (c): Unflooded Stevns Klint chalk; (d): Aalborg core AA21 flooded with NaCl (slice 7); (e): Aalborg core AA5 flooded with $MgCl_2$ (slice 2); (f): Kansas core KA8 flooded with $MgCl_2$ (slice 1). 'C': Coccoliths are observed in all unflooded samples (indicated by pink arrows). 'O': Opal–CT lepispheres were spotted in Aalborg (marked by yellow square). 'Si–Mg': Si–Mg–bearing minerals were observed in AA5 (in dark blue), 'M': Magnesite is precipitated in $MgCl_2$ flooded cores (in red). The scale bar equals 4 micron.

3.1.2 *NaCl flooded cores*

Applied FEG–SEM (Sup. Mat. Fig. 2a–e) showed no indication of precipitation of any new minerals, in agreement with earlier studies (Madland et al. 2011). The calcite grains observed near the inlet, appear somewhat corner–rounded compared to unflooded material (see Fig. 9a (AA21, slice 1) and Sup. Mat. Fig. 1d; unflooded Aalborg material). In AA21, opal–CT was not observed near the inlet but found preserved further inside the flooded core (Fig. 3d, yellow square; Fig. 11b, c). Euhedral microfossils could still be observed in all the tested chalk types.

3.1.3 *$MgCl_2$ flooded cores*

(Sup. Mat. Fig. 3) shows FEG–SEM images from the $MgCl_2$ flooded cores. For all chalk types the calcite grains appear corner–rounded, indicative for dissolution, although intact microfossils and coccolithophores can still be observed. The images also clearly reveal that crystals in hexagonal or trigonal shape, magnesite $MgCO_3$, have precipitated (Fig. 3e, f, red circles). In MO10, LI1, AA5 and SK6 euhedral magnesite crystals were not detected from slice 4 and towards the outlet, although geochemistry indicated MgO wt% between 2 and 9 times the average of unflooded material in those slices, (see Table 6a and c in 3.4). For KA8, euhedral magnesite crystals could only be found in slice 1 (Fig. 3f, inlet of KA8). Si–Mg–rich minerals in flake shape was found spread along the AA5 core (see Fig. 3e, Fig. 9e, f, green circle).

3.2 X–Ray Diffraction (XRD)

3.2.1 *Unflooded samples*

Chalk material from Kansas contains calcite, traces of quartz and phyllosilicates (peak at 4.44 ~ 4.50 Å, Sup. Mat. Fig. 4a) such as the clay minerals illite, illite/smectite and kaolinite (Sup. Mat. Fig. 4b). Mons chalk contains almost pure calcite (Sup. Mat. Fig. 4a); traces of quartz were identified along with poorly ordered illite/smectite (Sup. Mat. Fig. 4b). The chalk from Liège appears homogeneous in XRD studies: besides calcite, only traces of quartz and feldspar can be identified (Sup. Mat. Fig. 4a). The clays are dominated by smectite, and minor illite (Sup. Mat. Fig. 4b). Aalborg chalk contains dominant calcite with scarce quartz, very scarce opal–CT and gibbsite and traces of illite/smectite (Fig. 4a, Sup. Mat. Fig. 4b). The chalk sample from Stevns Klint differs from the other chalks because it is composed of almost pure calcium carbonate minerals, both calcite and Mg–calcite (Sup. Mat. Fig. 4a). Only traces of smectite with minor illite and quartz are observed (Sup. Mat. Fig. 4b).

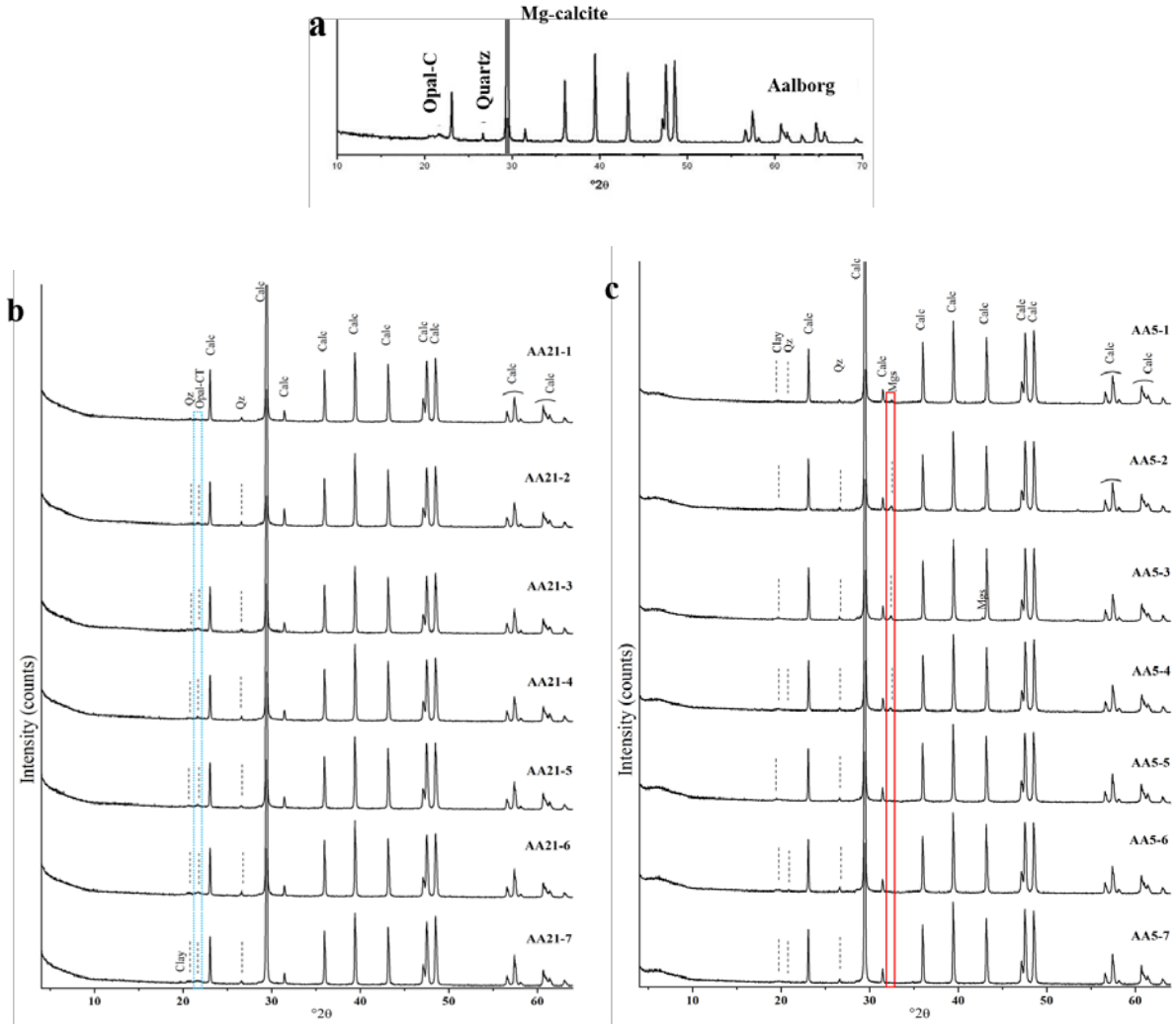

Fig. 4 XRD profiles (a): Material from unflooded Aalborg chalk; (b): NaCl flooded AA21 (slice 1 to 7); (c): $MgCl_2$ flooded AA5 (slice 1 to 7). Opal–CT is marked in blue dotted line. Magnesite is marked in red solid line. Remaining peaks marked 'Cal', 'Clay' and 'Qz' represent calcite, clay and quartz minerals, respectively.

3.2.2 *NaCl flooded cores*

There are no new grown minerals observed in the NaCl flooded cores (Sup. Mat. Fig. 5, XRD analysis of slice 3 of each core). The description is reported in Table 4.

Table 4 Mineralogical analysis of XRD profiles for NaCl and $MgCl_2$ flooded cores

Core	Mineralogical description in NaCl flooded cores	Core	Mineralogical description in $MgCl_2$ flooded cores
KA6	NO new grown minerals	KA8	Magnesite was more abundant than in the other flooded chalks. Magnesite was more abundant in slice 1 than the other slices, diminishing progressively, but still noticeable in traces in slice 6.
MO12	NO new grown minerals	MO10	Magnesite was identified in increasing amounts from slice 1 to slice 3, diminishing from slice 3 to 6 (only traces in this slice).
LI2	NO new grown minerals	LI1	Magnesite was observed in slice 1, 3 and 4, with most in slice 3, but not in the remaining slices. Traces of high–Mg calcite were found in slice 4.
AA21	NO new grown minerals	AA5	Scarce to minor magnesite was identified in slices 1 to 5 with a maximum in slices 2 and 3.
SK2	NO new grown minerals	SK6	Magnesite was identified in increasing amounts from slice 1 to slice 3, diminishing from slice 3 to 6 (only traces in slice 6).

3.2.3 *$MgCl_2$ flooded cores*

All chalks flooded with $MgCl_2$ contain different proportions of magnesite, always exhibiting broad XRD peaks denoting the small crystal size of this mineral. Sup. Mat. Fig. 6a, b show an XRD comparison of slice 1 (inlet) and slice 3 from the $MgCl_2$ flooded cores. The analysis indicated more magnesite in slice 3 than slice 1 in all cases except KA8, which had the strongest magnesite peak in slice 1. Quartz was identified in all cores (as in unflooded material).

The Kansas core (KA8) was characterized by a higher content of magnesite compared to the other flooded chalks. Another important difference is that magnesite was more abundant in slice 1 than the other slices (Sup. Mat. Fig. 6a, b) and its XRD peak intensities diminishing progressively in the other slices, however traces could still be found in slice 6. In the Mons core (MO10) magnesite was identified in increasing amounts from slice 1 to slice 3 (Sup. Mat. Fig. 6a, b), diminishing from slice 3 to 6 (only traces in this slice). In the Liège core (LI1) the XRD analysis identified the largest amount of magnesite in slice 3. Magnesite was also identified in slices 1 and 4, but not in the remaining slices. Traces of high–Mg calcite (Brindley and Brown 1980) were found in slice 4 (Sup. Mat. Fig. 6a, b). In the AA5 core (Fig. 4c) scarce to minor

magnesite was identified in slices 1 to 5 with maximum amount in slices 2 and 3. Opal–CT, which was widespread in unflooded Aalborg chalk was not identified in AA5 by XRD after flooding (Fig. 4c). The Stevns Klint core (SK6) gave similar observations as MO10. Magnesite was identified in increasing amounts from slice 1 to slice 3, diminishing from slice 3 to 6 (only traces in this slice), but slice 1 of SK6 contained more magnesite than slice 1 of MO10 (Sup. Mat. Fig. 6a, b).

3.3 Automated SEM Mineral Liberation Analysis (SEM–MLA)

SEM–MLA involving EDX spectral mapping (GXMAP mode) was applied on unflooded material and slices 1, 3, and 7 of flooded cores with flooded surfaces to interpret the mineralogical changes. The results are summarized in Table 5.

3.3.1 *Unflooded samples*

MLA analyses confirmed the mineralogical properties of unflooded chalk as described above. An MLA–image of unflooded Aalborg chalk is given in Fig. 5a. Images of the other samples can be found in Sup. Mat. Fig. 7. Calcite was the dominant mineral. Quartz could also be detected (grey grains in Fig. 7a) in qualitatively larger amounts for Liège and Aalborg compared to Kansas, Mons and Stevns Klint. MLA also detected clay minerals: Illite and/or chlorite in all samples; kaolinite in Kansas and Mons; glauconite was detected in Kansas, Mons, Liège and Stevns Klint; apatite was observed in Mons, Aalborg and Stevns Klint. In Aalborg chalk, more microfossils could be observed than for other chalk material. The EDX spectral mapping did not discriminate opal–CT from other Si–bearing phases such as quartz. These phases can be distinguished by their crystallographic properties in X–ray diffraction, but not by their equivalent elemental compositions (Si, O). Also, due to small particle sizes of the Si–O bearing phases like opal–CT, the electron beam will excite neighbouring grains like calcite, producing socalled mixed spectra, such as ‘Calcite–Si mix’, etc.

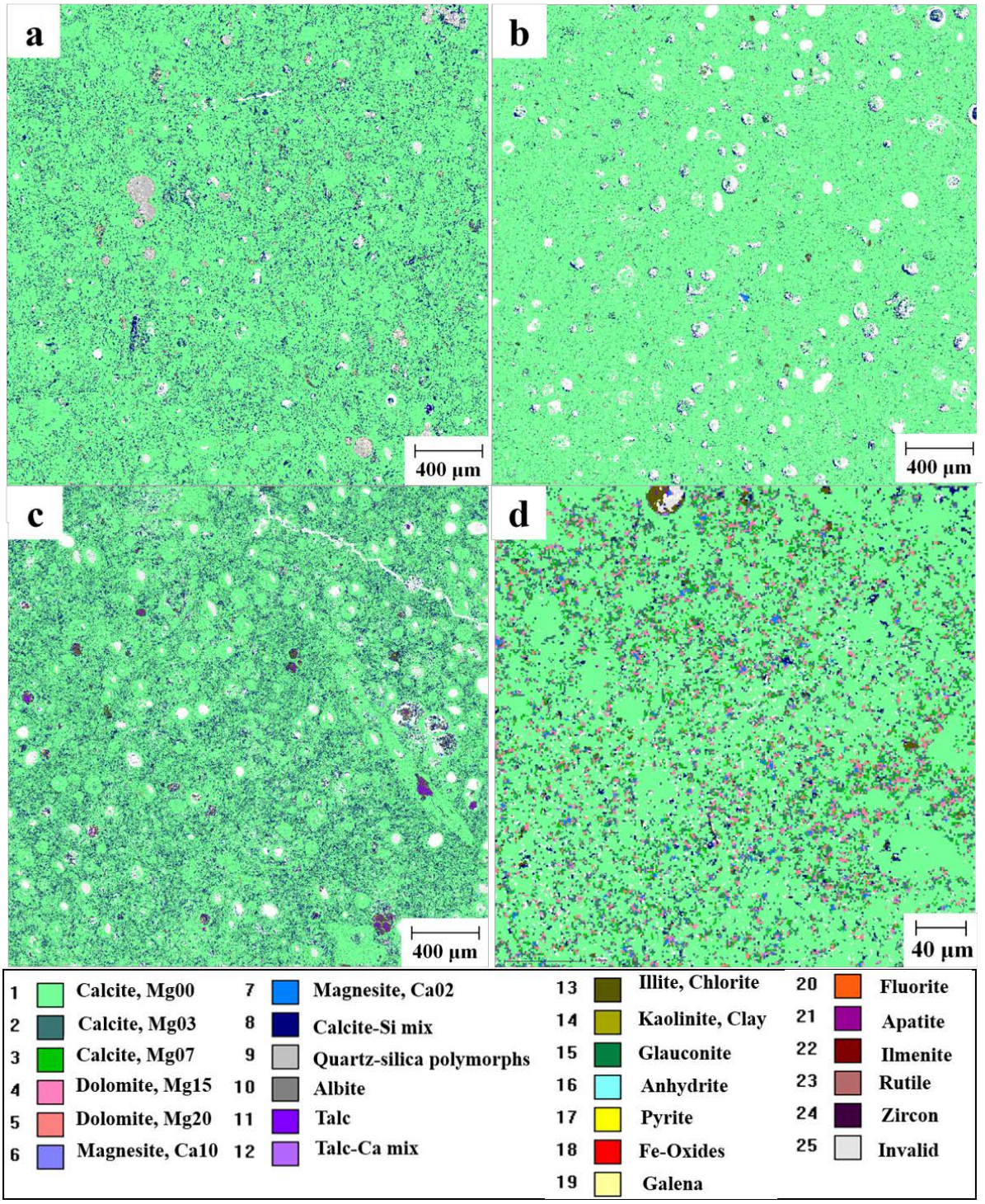

Fig. 5 MLA images (a): unflooded Aalborg chalk; (b): NaCl flooded AA21 (slice 1); (c): $MgCl_2$ flooded AA5 (slice 1); (d): $MgCl_2$ flooded KA8 (slice 1). 'bright green'–calcite, 'bright blue'–magnesite, 'pink'–dolomite, 'purple'–talc. Element content information in the legend refers to quantified EDX–spectra, e.g. Calcite–Mg10 corresponds to calcite with up to 10 wt% Mg.

3.3.2 *NaCl flooded cores*

No significant new minerals were observed in NaCl flooded material, see Table 5 for results from slice 1 of each chalk type. Calcite and non–carbonate phases like quartz, illite/chlorite, apatite, kaolinite, and glauconite could still be found, as in unflooded material (Table 5). Fig.

5a shows an MLA image of unflooded Aalborg chalk. In addition to a dominant green (calcite indication) a dense pattern of dark blue spots ('Calcite–Si mix') is seen, likely representing opal–CT or quartz mineral phases mixed with calcite. Considering Fig. 5b of slice 1 from AA21 (flooded with NaCl) the dark blue spots are much less abundant, implying that these phases have been partly removed, either by transport or dissolution processes. Microfossils can still be observed in their nearly original shape, but several of them with open pore space. Some have dark blue accumulations of 'Calcite–Si mix' where this phase could have been redeposited or re–precipitated during flooding. More images of NaCl flooded samples can be found in Sup. Mat. Fig. 8a–c.

Table 5 Mineralogical analysis of MLA images for unflooded end piece material and NaCl and $MgCl_2$ flooded cores.

Unflooded material	MLA interpretation	NaCl flooded cores	MLA interpretation	$MgCl_2$ flooded cores	MLA interpretation
KA	Calcite–Mg, calcite–Si mix, magnesite, dolomite, quartz–silica polymorphs, glauconite, illite and/or chlorite, kaolinite and/or clay	KA6	KA6–1: Calcite–Mg, calcite–Si mix, magnesite, dolomite, quartz–silica polymorphs, glauconite, illite and/or chlorite, kaolinite and/or clay	KA8	KA8–1: Calcite–Mg, calcite–Si mix, magnesite, dolomite, quartz–silica polymorphs, illite and/or chlorite KA8–3: Calcite–Mg, calcite–Si mix, magnesite, dolomite, quartz–silica polymorphs, illite and/or chlorite KA8–7: Calcite–Mg, calcite–Si mix, dolomite, quartz–silica polymorphs, apatite, illite and/or chlorite,
MO	Calcite–Mg, calcite–Si mix, apatite, quartz–silica polymorphs, glauconite, illite and/or chlorite, kaolinite and/or clay	MO12	MO12–1: Calcite–Mg, calcite–Si mix, quartz–silica polymorphs, glauconite, apatite, illite and/or chlorite, kaolinite and/or clay	MO10	No data
LI	Calcite–Si mix, dolomite, quartz–silica polymorphs, glauconite, illite and/or chlorite	LI2	LI2–1: Calcite–Si mix, dolomite, quartz–silica polymorphs, glauconite, illite and/or chlorite	LI1	LI1–1: Calcite–Mg, calcite–Si mix, magnesite, dolomite, quartz–silica polymorphs, apatite, illite and/or chlorite LI1–3: Calcite–Mg, calcite–Si mix, magnesite, dolomite, quartz–silica polymorphs, apatite, illite and/or chlorite LI1–7: Calcite–Mg, calcite–Si mix, dolomite, quartz–silica polymorphs, apatite, illite and/or chlorite

AA	Calcite–Mg, calcite–Si mix, quartz–silica polymorphs, apatite, illite and/or chlorite	AA21	AA21–1: Calcite–Mg, calcite–Si mix, quartz–silica polymorphs, apatite, illite and/or chlorite	AA5	AA5–1: Calcite–Mg, magnesite, dolomite, quartz–silica polymorphs, talc, illite and/or chlorite AA5–3: Calcite–Mg, calcite–Si mix, magnesite, dolomite, quartz–silica polymorphs, apatite, talc, illite and/or chlorite AA5–7: Calcite–Mg, calcite–Si mix, magnesite, dolomite, quartz–silica polymorphs, apatite, talc, illite and/or chlorite
SK	Calcite–Mg, calcite–Si mix, quartz–silica polymorphs, glauconite, apatite, illite and/or chlorite	SK2	SK2–1: Calcite–Mg, calcite–Si mix, quartz–silica polymorphs, glauconite,apatite, illite and/or chlorite	SK6	SK6–1: Calcite–Mg, calcite–Si mix, magnesite, dolomite, quartz–silica polymorphs, illite and/or chlorite SK6–3: Calcite–Mg, calcite–Si mix, magnesite, dolomite, quartz–silica polymorphs, illite and/or chlorite SK6–7: Calcite–Mg, calcite–Si mix, dolomite, quartz–silica polymorphs, illite and/or chlorite

3.3.3 *$MgCl_2$ flooded cores*

SEM–MLA detected significant changes in the $MgCl_2$ flooded cores (data from MO10 was not available). As for unflooded samples, calcite and quartz were indicated. In addition, all cores indicated magnesite (bright blue colour) and dolomite (pink colour) in slice 1, as seen in Fig. 5c–d (AA5 and KA8) and Sup. Mat. Fig. 9a, b (LI1 and SK6). AA5, KA8 and SK6 indicated more precipitation of dolomite (pink colour) and magnesite (bright blue colour) than LI1. In AA5, talc was indicated in slice 1 (Fig. 5c, purple colour), 3 (to lesser extent) and 7, as a new mineral phase not observed in unflooded material or the other chalks. The microfossils in AA5, slice 1, appear to be filled with newly formed minerals, i. e. talc, or partly dissolved with pore space left. Illite and/or chlorite could still be found in the five cores after flooding. Kaolinite (observed in unflooded Kansas material) could not be observed in KA8 after flooding.

3.4 Geochemistry

3.4.1 *Unflooded samples*

The geochemical analysis of untested chalk is summarized in Table 6a (the complete data set is in Sup. Mat. Table 1 together with details of detection limits). These statistics are based on 5 to 9 cores of each chalk type to indicate natural compositional variations.

Table 6 Geochemical analysis of (a) unflooded end piece material from several different cores of same chalk type summarized by average and standard deviation (data from each core is given in Sup. Mat. Table 1), (b) unflooded end piece material and flooded slices from NaCl flooded cores and (c) unflooded end piece material and flooded slices from $MgCl_2$ flooded cores. The abbreviations are 'PPM' – part per million, 'wt%' – weight percent, 'TOT/C' – total carbon, 'SD' – standard deviation, 'b. d. l.' – below detection limit and 'I.S.' – no valid measurement. The exact sampling position of the unflooded material relative to the core samples is shown in Fig. 1a.

a) Unflooded chalk	**SiO_2 (wt%)**	**Al_2O_3 (wt%)**	**MgO (wt%)**	**CaO (wt%)**	**K_2O (wt%)**	**Rb (PPM)**	**Sr (PPM)**	**Zr (PPM)**	**TOT/C (wt%)**
Kansas average	1.23	0.36	0.23	54.66	0.09	2.3	895.6	6.6	12.1
SD	0.17	0.08	0.02	0.34	0.01	0.6	37.3	0.8	0.2
Mons average	0.98	0.24	0.27	55.02	0.07	2.2	828.7	3.8	12.2
SD	0.06	0.03	0.02	0.08	0.02	0.4	30.7	1.4	0.1
Liège average	1.98	0.34	0.27	54.17	0.08	3.2	947.6	7.3	12.0
SD	0.13	0.03	0.02	0.17	0.01	0.5	32.8	1.1	0.1
Aalborg average	5.06	0.35	0.42	52.10	0.09	3.1	736.8	5.2	11.7
SD	0.84	0.05	0.02	0.65	0.01	0.4	42.5	0.8	0.2
Stevns Klint average	0.37	0.08	0.29	55.59	0.02	0.8	1165.3	2.4	12.3
SD	0.04	0.02	0.01	0.15	<0.01	0.2	40.8	1.1	0.2
b) NaCl flooded chalk cores	**SiO_2 (wt%)**	**Al_2O_3 (wt%)**	**MgO (wt%)**	**CaO (wt%)**	**K_2O (wt%)**	**Rb (PPM)**	**Sr (PPM)**	**Zr (PPM)**	**TOT/C (wt%)**
KA6 (unflooded)	1.50	0.50	0.20	54.20	0.10	3.3	842.2	7.0	11.9
KA6–1	1.20	0.40	0.20	54.00	0.10	1.5	918.0	8.9	12.1
KA6–2	1.50	0.50	0.20	53.50	0.10	2.4	910.2	7.8	11.9
KA6–3	1.60	0.50	0.20	54.20	0.10	2.9	988.3	8.2	12.2
KA6–4	1.60	0.50	0.20	54.00	0.10	2.9	1015.3	8.1	12.4
KA6–5	1.80	0.60	0.20	53.70	0.10	3.2	984.9	8.8	12.1
KA6–6	1.70	0.60	0.20	53.60	0.10	3.2	1025.1	8.6	12.1
KA6–7	1.70	0.60	0.20	53.70	0.10	3.4	1061.5	8.4	12.1
MO12 (unflooded)	1.00	0.20	0.30	55.10	0.10	2.3	874.3	5.2	12.0
MO12–1	0.70	0.20	0.27	56.20	0.00	1.6	935.5	3.1	12.3
MO12–2	0.90	0.20	0.26	55.20	0.10	1.8	874.0	3.0	12.4
MO12–3	0.90	0.30	0.26	55.30	0.10	2.0	903.1	3.3	12.2
MO12–4	0.90	0.30	0.25	54.70	0.10	2.0	970.0	2.9	12.5
MO12–5	1.00	0.30	0.25	54.70	0.10	2.2	944.5	2.9	12.4
MO12–6	0.90	0.30	0.26	56.50	0.10	1.9	938.5	2.9	12.4
MO12–7	1.00	0.30	0.24	57.40	0.10	2.1	944.0	3.4	12.4
LI2 (unflooded)	1.90	0.30	0.30	54.10	0.10	3.6	910.4	8.2	11.8
LI2–1	1.40	0.30	0.30	54.40	0.00	1.8	1042.7	8.1	12.5
LI2–2	1.80	0.40	0.30	55.50	0.10	2.1	1039.2	5.7	12.7
LI2–3	1.80	0.30	0.30	55.70	0.10	1.9	1033.9	5.6	12.7
LI2–4	2.00	0.40	0.30	54.70	0.10	2.3	1019.8	7.8	12.8
LI2–5	2.00	0.40	0.30	54.10	0.10	2.7	947.0	9.3	12.5
LI2–6	2.00	0.40	0.30	54.20	0.10	2.5	968.0	8.6	12.6

LI2–7	2.10	0.40	0.30	53.80	0.10	2.8	997.3	9.0	12.8
AA21 (unflooded)	5.00	0.30	0.40	52.10	0.10	2.9	817.6	6.1	11.6
AA21–1	2.40	0.30	0.50	53.90	0.00	1.6	783.1	4.3	12.1
AA21–2	2.40	0.40	0.50	53.60	0.00	1.5	774.0	7.0	12.1
AA21–3	4.50	0.40	0.50	52.40	0.10	2.3	776.3	5.5	11.9
AA21–4	6.00	0.50	0.40	51.20	0.10	3.1	820.6	7.9	11.5
AA21–5	4.40	0.40	0.50	52.20	0.10	2.6	769.6	7.1	11.6
AA21–6	6.10	0.50	0.40	51.00	0.10	3.1	834.0	7.4	11.6
AA21–7	5.90	0.40	0.40	51.50	0.10	3.0	793.0	6.5	11.5
SK2 (unflooded)	0.40	0.10	0.30	55.60	b.d.l.	1.0	1090.1	3.3	12.3
SK2–1	0.20	0.10	0.40	56.00	b.d.l.	b.d.l.	1133.5	2.6	12.7
SK2–2	0.20	0.00	0.30	56.10	b.d.l.	b.d.l.	1137.6	3.2	13.1
SK2–3	0.20	0.10	0.30	55.70	b.d.l.	b.d.l.	1160.0	2.3	12.9
SK2–4	0.20	0.10	0.30	55.80	b.d.l.	b.d.l.	1197.7	2.7	12.8
SK2–5	0.20	0.10	0.30	55.70	b.d.l.	0.1	1197.3	3.0	12.8
SK2–6	0.20	0.00	0.30	55.90	b.d.l.	0.2	1197.4	1.3	12.9
SK2–7	0.20	0.00	0.30	55.90	b.d.l.	b.d.l.	1168.9	0.8	12.9
c) $MgCl_2$ flooded chalk cores	**SiO_2 (wt%)**	**Al_2O_3 (wt%)**	**MgO (wt%)**	**CaO (wt%)**	**K_2O (wt%)**	**Rb (PPM)**	**Sr (PPM)**	**Zr (PPM)**	**TOT/C (wt%)**
KA8 (unflooded)	1.30	0.30	0.20	54.50	0.10	2.0	932.9	7.7	12.0
KA8–1	1.20	0.40	6.50	46.40	0.00	1.5	763.2	6.0	12.3
KA8–2	1.10	0.30	3.70	50.50	0.00	1.4	830.0	10.7	12.1
KA8–3	1.10	0.30	1.80	52.70	0.00	1.4	880.9	6.5	11.9
KA8–4	1.10	0.30	1.30	53.50	0.00	1.5	928.3	6.2	12.1
KA8–5	1.10	0.30	1.00	53.70	0.00	1.3	911.2	5.7	12.1
KA8–6	1.10	0.30	0.90	54.10	0.00	1.4	927.2	6.1	11.7
KA8–7	1.00	0.30	0.80	54.00	0.00	1.2	886.8	5.4	12.2
MO10 (unflooded)	0.90	0.20	0.30	55.10	0.10	2.2	871.1	2.6	12.3
MO10–1	1.00	0.30	1.31	53.60	0.10	2.3	980.9	3.2	11.9
MO10–2	1.00	0.30	2.26	52.90	0.10	2.4	964.8	3.1	12.1
MO10–3	1.00	0.30	2.51	54.00	0.00	2.1	933.7	3.0	12.6
MO10–4	0.80	0.20	1.64	53.40	0.00	2.0	939.9	3.4	12.3
MO10–5	0.90	0.20	1.08	54.60	0.00	2.0	914.2	3.3	12.3
MO10–6	0.80	0.20	0.84	54.40	0.00	1.9	890.4	3.4	12.2
MO10–7	0.90	0.20	0.79	57.90	0.00	1.8	914.6	2.9	12.0
LI1 (unflooded)	2.20	0.40	0.30	54.00	0.10	2.2	994.9	5.2	11.9
L1–1	1.70	0.30	1.70	52.80	0.00	2.5	1007.2	7.2	11.9
L1–2	2.00	0.40	2.30	51.50	0.10	2.6	957.6	7.5	12.1
L1–3	2.10	0.40	3.20	50.80	0.10	2.7	891.4	8.9	12.5
L1–4	2.10	0.40	2.10	51.90	0.10	3.1	921.6	10.0	12.4
L1–5	2.10	0.40	1.40	52.60	0.10	2.9	963.3	11.5	12.7
L1–6	2.10	0.40	1.20	53.20	0.10	2.7	1008.0	11.0	12.6
L1–7	2.00	0.40	1.00	53.40	0.10	2.6	978.4	10.4	12.4
AA5 (unflooded)	4.00	0.30	0.40	53.00	0.10	2.8	691.6	5.2	11.9

AA5–1	3.80	0.40	3.20	50.20	0.00	1.8	680.3	5.5	11.8
AA5–2	4.10	0.40	3.60	49.40	0.10	2.0	714.3	4.9	11.6
AA5–3	3.70	0.30	3.30	50.00	0.00	1.9	663.4	4.1	11.8
AA5–4	4.30	0.30	2.80	50.30	0.00	1.8	720.2	5.1	11.6
AA5–5	5.30	0.50	2.90	49.50	0.10	3.1	790.9	6.0	11.3
AA5–6	5.20	0.40	2.60	49.70	0.10	3.0	782.6	8.6	11.4
AA5–7	6.20	0.50	2.60	49.30	0.10	3.4	839.0	7.5	11.2
SK6 (unflooded)	0.30	0.10	0.30	55.30	b.d.l.	0.8	1166.6	2.0	12.1
SK6–1	I.S.	I.S.	I.S.	I.S.	I.S.	0.3	1162.4	2.2	12.2
SK6–2	I.S.	I.S.	I.S.	I.S.	I.S.	0.2	1124.9	1.6	12.4
SK6–3	0.40	0.10	2.90	51.80	b.d.l.	b.d.l.	1105.8	1.6	12.3
SK6–4	0.40	0.10	2.20	52.50	b.d.l.	0.2	1150.0	1.6	12.3
SK6–5	0.40	0.10	1.20	53.80	b.d.l.	0.3	1031.0	2.1	12.2
SK6–6	0.40	0.10	0.80	54.50	b.d.l.	0.3	1016.4	1.8	12.2
SK6–7	0.30	0.10	0.60	54.60	b.d.l.	0.3	1019.5	1.7	12.4

The chalks are all, as expected dominated by CaO and they have low MgO concentrations (0.23 – 0.42 wt%) with total carbon around 12 %. Sr correlates in general positively with CaO. Trace element geochemistry does not point to any significant clastic input measured by Rb and Zr with values often below 5 ppm, which is 10 – 15 times below the typical upper continental crust composition (McLennan et al. 2006).

Chalk samples from Kansas (KA) contain CaO between 54.2 and 55.1 wt% and relatively small amounts of non–carbonate phases with content of SiO_2 between 1.1 and 1.5 wt% and minute K_2O (0.1 wt%) and Al_2O_3 between 0.3 and 0.5 wt%. Clastic input is as well minute with concentrations for Rb, Zr and Y, trace elements, which solely occur in clastic material, below 5 ppm. Chalk from Mons (MO) contains slightly lower SiO_2 (0.98 wt%) than chalk cores from Kansas with CaO straddling 55 wt%. With Al_2O_3 as low as 0.2 wt% and even lower trace element concentrations, this chalk type seems to be ‘cleaner’ than the cores from Kansas. Samples from Liège (LI) contain more SiO_2 comparable to Kansas chalk (KA). Concentrations of CaO are around 54 wt%, Al_2O_3 is around 0.3 wt% and values of Rb, Zr and Y are higher than in the above presented chalks point to slightly more clastic material. The Aalborg chalk samples (AA) show the highest amount of non–carbonate material compared to the other chalks. Therefore, CaO concentrations are lower between 51.4 and 53.0 wt% compared to all other chalks. SiO_2 is between 4 and 6 wt% and Al_2O_3 is only around 0.4 wt%, pointing to quartz or opal rather than more complex silicates. Chalk exposed at Stevns Klint (SK) is the cleanest one, with the lowest values of MgO and SiO_2. These samples contain CaO around 56 wt%.

3.4.2 *NaCl flooded cores*

For the NaCl flooded cores the whole–rock geochemical analysis revealed minor, but detectable changes compared to unflooded material (Table 6b). The major elements (Mg, Al, Na and K) vary only slightly along the core. The SiO_2 fraction generally decreased compared to unflooded material, except for KA6 where an increase was measured. The lowest content of SiO_2 was found in the inlet slice for all five cores (KA6, MO12, LI2, AA21 and SK2). In SK2 all slices show the same content of SiO_2 (0.2 wt%), which is roughly a factor 2 lower than unflooded material (0.4 wt%). In MO12 and LI2, when disregarding slice 1 (MO12: 0.7 wt%; LI2: 1.4 wt%), the SiO_2 measurements (average MO12: 0.9 wt%; LI2: 1.95 wt%) are close to the values from unflooded material (MO12: 1 wt%; LI2: 1.9 wt%). For KA6, all values (average 1.65 wt%) except the first slice (1.2 wt%) are higher than unflooded material content (1.5 wt%). The most pronounced changes were seen in AA21, where SiO_2 content showed a strong increasing trend from the inlet slice (2.4 wt%) to the outlet slice (5.9 wt%). From slices 1 to 3 and in slice 5 the values were lower than for unflooded material (5.0 wt%), while near the outlet (for slices 4, 6 and 7) the values were higher than that of unflooded material.

3.4.3 *$MgCl_2$ flooded cores*

The geochemical data of the $MgCl_2$ flooded cores are reported in Table 6c. The average SiO_2 content in KA8 and LI1 (respectively 1.1 wt% and 2.0 wt%) is moderately lower than unflooded material (KA:1.3 wt%; LI: 2.2 wt%), while for MO10 and SK6 the change was negligible (from 0.90 and 0.3 wt% in unflooded material to 0.91 and 0.38 wt%). The variations in silica for these samples seem to be related to natural variation rather than significant changes resulting from the tests. The SiO_2 content in AA5 after flooding (4.6 wt% on average) is lower than the average of unflooded Aalborg samples (5.1 wt%), with an increasing trend from the inlet (3.8 wt%) towards the outlet (6.2 wt%). Variations in wt% of Al_2O_3 and K_2O correlated positively with SiO_2 for Stevns Klint, Mons and Kansas chalks, which could indicate phyllosilicates and/or feldspar. The correlation was not significant for Liége and Aalborg, pointing to a more mixed composition. The different cores had very similar trace content of MgO before flooding (Table 6c), which in the different chalk samples increased significantly after flooding. KA8 has most of its MgO (6.5 wt%) in the inlet slice, with rapidly decreasing amounts towards the outlet (0.8 wt%). MO10 (from Mons) and LI1 (from Liège) are similar and show a peak (2.5 wt% and 3.2 wt%, respectively) of MgO increase in slice 3. AA5 has again a different characteristic with a rather uniform MgO distribution (between 2.6 wt% and 3.6 wt%) with the highest value (3.6 wt%) in slice 2 and then decreasing. SK6 unfortunately lacks data from slices 1 and 2, but shows decreasing MgO amounts from slice 3 (2.9 wt%) towards the outlet (0.6 wt%).

3.5 Stable isotope geochemistry

3.5.1 *Unflooded samples*

C and O isotope measurements of unflooded material and flooded core material are given in Sup. Mat. Table 2. The unflooded samples were very homogeneous. The isotope parameters $\delta^{13}C_{SMOW}$ and $\delta^{18}O_{SMOW}$ were mostly in the range 1.5 to 2.1 ‰ and −1.9 to −1 ‰, respectively, for all chalks except for samples from Kansas ($\delta^{13}C_{SMOW}$ and $\delta^{18}O_{SMOW}$ on average 0.2 ‰ and −5 ‰, respectively). All measured values for $\delta^{13}C_{SMOW}$ and $\delta^{18}O_{SMOW}$ from Mons (on average: 2 ‰ and −1.7 ‰, respectively), Liège (on average: 1.5 ‰ and −1.9 ‰, respectively), Aalborg (on average: 2.1 ‰ and −1.2 ‰, respectively) and Stevns Klint (on average: 1.6 ‰ and −1.6 ‰, respectively) seem to be primarily reflecting global isotope excursions. An exception are the samples from Kansas, their oxygen isotope ratios are strongly altered and do not reflect primary compositions.

3.5.2 *NaCl flooded cores*

In NaCl flooded cores, $\delta^{13}C_{SMOW}$ values are almost the same as for untested material and observed variations are natural ones. $\delta^{18}O_{SMOW}$ is also comparable to unflooded material, but the values are slightly more negative in the flooded cores MO12 (−2.2 ‰), SK2 (−1.9 ‰) and KA6 (−5.1 ‰).

3.5.3 *$MgCl_2$ flooded cores*

In the $MgCl_2$ flooded cores, $\delta^{13}C_{SMOW}$ was also almost the same as for untested material, while $\delta^{18}O_{SMOW}$ values tended to be slightly more negative (MO10: −2.0 ‰; LI1: −2.0 ‰; AA5: −1.2 ‰; SK6: −1.8 ‰; KA8: −5.3‰).

3.6 Mass measurements

As described (see 2.2.1), the dry weight of the applied cores was measured before ($M_{dry,o}$) and after ($M_{dry,end}$) flooding and the difference $\Delta M = M_{dry,end} - M_{dry,o}$ was calculated along with the average rate of mass changes $\Delta M/\Delta t$, see results in Table 7. In all tests the cores experienced a net mass loss. The NaCl flooded cores KA6, MO12, and LI2 lost 0.5 to 0.6 g, SK2 had a smaller loss of 0.16 g, while AA21 had a comparatively large mass reduction of 1.51 g. With $MgCl_2$ flooding, the purest chalk cores (SK1: 1.71 g; SK6: 1.11 g; MO10: 1.57 g) obtained a lower mass loss than the more impure chalk cores (LI1: 2.1 g; KA8: 1.86 g), with especially high mass reduction in the Aalborg cores (AA1: 5.14 g; AA5: 4.15 g). The mentioned trends were similar when normalizing for flooding time (i.e. mass rate) although the distinction between the $MgCl_2$ flooded cores became less apparent (between −0.02 and −0.04 g/d), except for the

Aalborg cores AA5 and AA1 standing out with a high mass rate (–0.045 to –0.067 g/d). Note that the mass change of the cores were on the order of ~ 0.1 % of the original mass for some of the NaCl flooded cores, and thus very sensitive to unaccounted losses, e.g. during unloading or to remaining fluid after drying.

Table 7 Dry mass $M_{dry,end}$ (g) after flooding, mass change $\Delta M = M_{dry,end} - M_{dry,o}$ (g) compared to original state and corresponding average mass rate of the core $\Delta M/\Delta t$ (g/d).

NaCl flooded cores				$MgCl_2$ flooded cores			
Core	$M_{dry,end}$ (g)	ΔM (g)	$\Delta M/\Delta t$ (g/d)	Core	$M_{dry,end}$ (g)	ΔM (g)	$\Delta M/\Delta t$ (g/d)
KA6	134.40	–0.50	–0.008	KA8	134.38	–1.86	–0.025
MO12	123.92	–0.60	–0.010	MO10	124.01	–1.57	–0.026
LI2	125.51	–0.54	–0.006	LI1	110.28	–2.10	–0.032
AA21	111.45	–1.51	–0.025	AA5	108.18	–4.15	–0.067
SK2	121.15	–0.16	–0.002	AA1*	114.7	–5.14	–0.045
				SK6	113.97	–1.11	–0.018
				SK1*	115.70	–1.71	–0.038

3.7 Mechanical tests – hydrostatic loading and creep compaction

The axial stress plotted *versus* strain from the loading phase is given in Fig. 6, with corresponding yield points (stress at which nonlinear deformation initiates) and bulk moduli in Table 8. Cores of same chalk type obtained similar bulk modulus regardless of the brines and there were no direct trends between the given brines and yield points. This is in agreement with (Madland et al. 2011; Megawati et al. 2015). A general trend was that higher (initial) porosity cores displayed lower yield point and bulk modulus (see Sup. Mat. Fig. 10), consistent with Engstrøm (1992) and Havmøller and Foged (1996). Kansas was the strongest chalk, followed by Mons. The rest behaves similarly and the yield points are mainly between 5 and 8 MPa. SK1 is the weakest core, with yield point at 4.8 MPa.

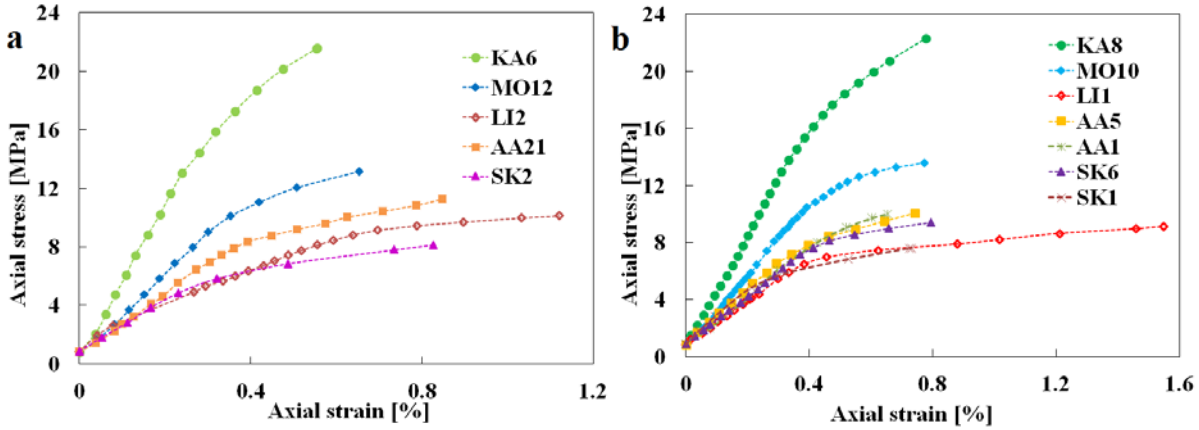

Fig. 6 Axial stress *versus* axial strain obtained during hydrostatic loading for the NaCl (a) and $MgCl_2$ (b) flooded cores.

Table 8 Yield point (MPa) and bulk modulus (GPa) of the different cores as determined during the loading phase.

Core	Brine	Yield point (MPa)	Bulk modulus (GPa)	Confining pressure during creep (MPa)
KA6	NaCl	13.0	0.69	23.0
KA8	$MgCl_2$	15.4	0.51	23.0
MO12	NaCl	9.0	0.38	14.0
MO10	$MgCl_2$	10.5	0.34	14.0
LI2	NaCl	7.4	0.18	10.5
LI1	$MgCl_2$	6.5	0.23	9.5
AA21	NaCl	7.9	0.27	12.0
AA5	$MgCl_2$	7.2	0.26	11.0
AA1*	$MgCl_2$	7.9	0.24	11.0
SK2	NaCl	5.8	0.22	8.5
SK6	$MgCl_2$	7.6	0.23	10.0
SK1*	$MgCl_2$	4.8	0.27	8.5

The creep strain development (compaction under constant stress) for the five NaCl flooded cores is shown in Fig. 7a. The strain rate is gradually decreasing throughout the tests. In the case of SK2, the piston did not move smoothly during the first 25 days, resulting in somewhat erroneous measurements. Interestingly, AA21 with highest porosity (46.7 %) compacted the least.

Creep compaction profiles for $MgCl_2$ injected cores are shown in Fig. 7b. Note that two Stevns Klint cores (SK1 and SK6) and two Aalborg cores (AA1 and AA5) were used in order to check the reproducibility of the compaction behaviour. These chalk types, respectively contained least and most non–carbonate content, see Table 6a and c. The Aalborg cores (AA1 and AA5) compacted the most, with a continuously decreasing compaction rate. The cores MO10, LI1,

SK6 and SK1 shared another type of behaviour: The initial few days the strain rate was high, followed by a period of slow compaction (lasting up to ~ 24 d for MO10, ~ 28 d for LI1, ~ 14 d for SK6 and ~ 6 d for SK1). The compaction then accelerated, initiating a new period of continuous compaction with similar creep rate as the Aalborg cores (AA5 and AA1). KA8 also displayed a behaviour initial rapid compaction, followed by a low strain rate, and increased compaction rate after ~ 8 d. Compared to the four aforementioned cores, this core compacted the least in axial creep in the long run, likely due to its lower original porosity compared to the other cores (37 %, see Table 2), i.e. it had less volume for the grains to reorganize in. These observations agreed to a wide extent with previous results (Madland et al. 2011; Megawati et al. 2015), in which accelerated creep for the pure chalks Mons and Stevns Klint was observed after a certain period of time while Kansas, Liège and Aalborg cores compacted continuously from the very beginning. Their tests on Liège cores were stopped after 20.8 and 62.5 d (without seeing accelerated creep).

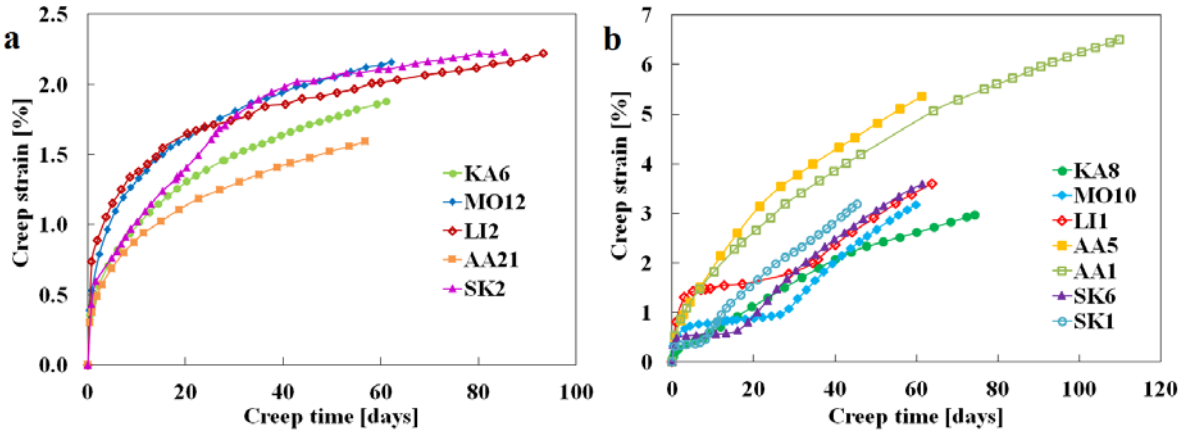

Fig. 7 Axial creep strain *versus* time profiles of the NaCl (a) and $MgCl_2$ (b) flooded cores. The NaCl flooded cores (a) display continuous compaction. The impure cores deformed less with NaCl flooding. The $MgCl_2$ flooded cores (b) display accelerated creep for pure cores (SK1, SK6, and MO10) and LI1. Note that the figures have different scales.

3.8 Effluent analysis of the flooded cores

In the NaCl flooding experiments, the produced concentrations of Cl^- and Na^+ were the same as injected (not shown), implying negligible chemical interaction from these ions. Fig. 8a shows that significant concentrations of Ca^{2+} were produced: Initial transient peaks (KA6: 0.002 mol/L; MO12: 0.007 mol/L; LI2: 0.014 mol/L; AA21: 0.009 mol/L; SK2: 0.004 mol/L) were observed. After 2 – 3 PVs injection, steady concentrations of Ca^{2+} followed (KA6: 0.001 mol/L; MO12: 0.001 mol/L; LI2: 0.003 mol/L; AA21: 0.004 mol/L; SK2: 0.002 mol/L). The peaks were 2 – 7 times the stable values. We note that the measurements were near or below the detection limit

(see Sup. Mat. 1.7). These transient (peak) and steady state observations indicate desorption and mineral dissolution processes (Madland et al. 2011, Andersen et al. 2012).

Fig. 8b shows the Ca^{2+} effluent measurements for $MgCl_2$ flooded cores. Concentration peaks between 0.033 mol/L (for SK6) and 0.055 mol/L (for KA8) are observed initially. KA8 and AA5 displayed a decreasing trend before stabilizing around and 0.036 mol/L and 0.024 mol/L, respectively. The cores MO10, LI1 and SK6 displayed Ca^{2+} concentration minima (Fig. 8b, MO10: 0.018 mol/L; LI1: 0.015 mol/L; SK6: 0.013 mol/L) before increasing again to stable levels (MO10: 0.027 mol/L; LI1: 0.017 mol/L; SK6: 0.022 mol/L). Mg^{2+} was retained inside all the tested cores, as seen in Fig. 8c with effluent Mg^{2+} concentrations clearly below the injected value (0.219 mol/L). This behaviour is equivalently opposite compared to the Ca^{2+} profile, i.e. the sum of produced Ca^{2+} and Mg^{2+} was stable and close to equal the injected concentration of 0.219 mol/L (not shown), consistent with (Madland et al. 2011; Megawati et al. 2015). As seen in Fig. 8c, KA8 and AA5 obtained increasing Mg^{2+} concentration trends initially which then stabilized around 0.184 mol/L and 0.195 mol/L, respectively, while the cores MO10, LI1 and SK6 showed Mg^{2+} concentration peaks (MO10: 0.205 mol/L; LI1: 0.216 mol/L; SK6: 0.215 mol/L) at the times when the Ca^{2+} concentrations reached their minima. Subsequently the Mg^{2+} effluent concentrations decreased and stabilized (MO10: 0.192 mol/L; LI1: 0.197 mol/L; SK6: 0.202 mol/L).

In addition to the mentioned ions, the Si^{4+} concentration profiles of AA21 and SK2 (flooded with NaCl) and AA5 and SK6 (flooded with $MgCl_2$) were measured by ICP–AES (Fig. 8d). Si^{4+} was produced, indicating dissolution of Si–bearing minerals in the cores, with effluent concentration ranging from 0.0003 mol/L to 0.0016 mol/L (low values compared with the Ca^{2+} concentrations). The Aalborg cores (which had high initial content of SiO_2, see Table 6) consistently produced more (concentrations between 0.0012 mol/L and 0.0016 mol/L) Si^{4+} than the SK cores (concentrations between 0.0003 mol/L and 0.0013 mol/L). A slightly higher production of Si^{4+} was observed in AA5 (flooded with $MgCl_2$, on average: ~0.0013 mol/L) compared with AA21 (flooded with NaCl, on average: ~0.0012 mol/L). The opposite was seen in SK cores where SK2 (flooded with NaCl, on average: ~0.0007 mol/L) produced some more Si^{4+} than SK6 (flooded with $MgCl_2$, on average: ~0.0004 mol/L).

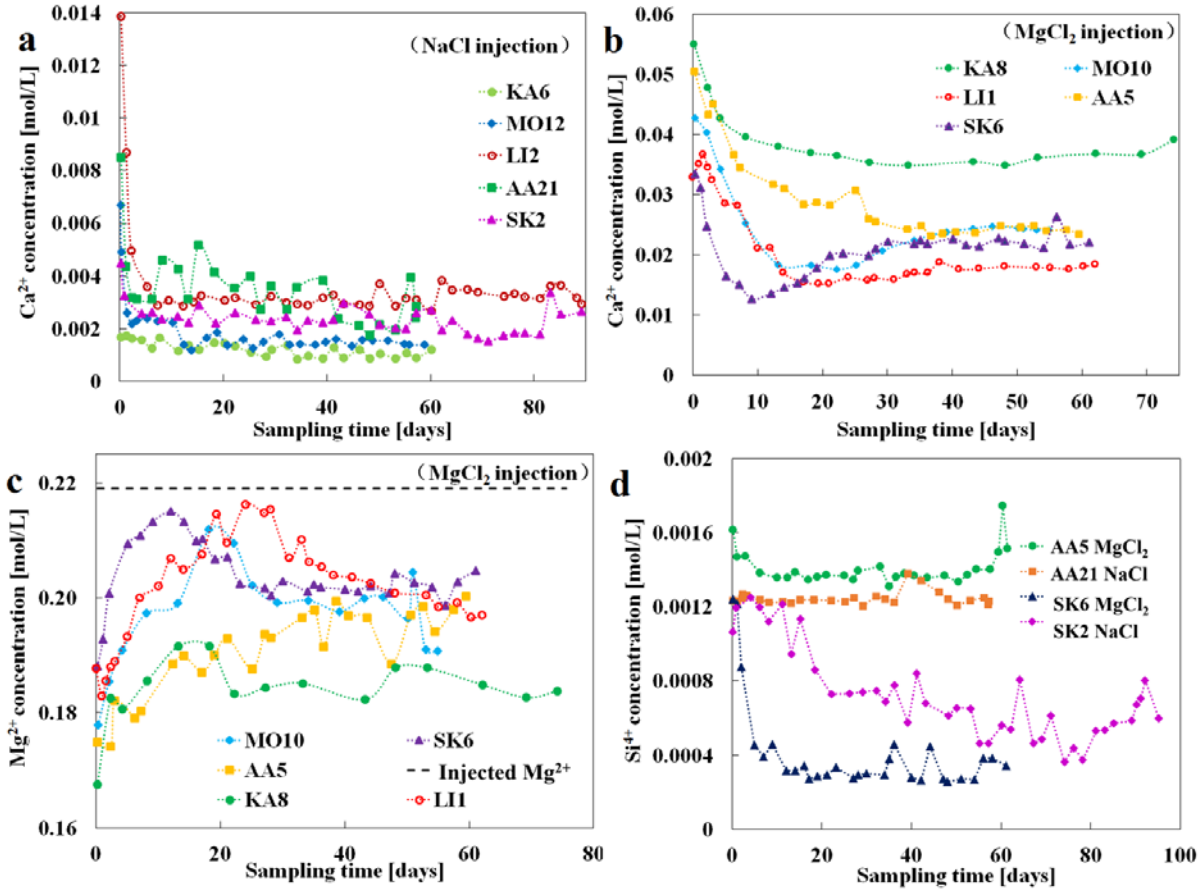

Fig. 8 Effluent analysis of the flooded cores. (a): Ca^{2+} concentration profiles in the effluent of NaCl flooded cores, (b): Ca^{2+} concentration profiles in the effluent of $MgCl_2$ flooded cores, (c):Mg^{2+} concentration profiles in the effluent of $MgCl_2$ flooded cores, (d): Si^{4+} concentration profiles in the effluent of the cores AA5, SK6 (flooded with $MgCl_2$), AA21 and SK2 (flooded with NaCl).

3.9 Solid density estimation

Table 9 shows the density values (ρ_{end}) from parts P1 and P2 and groups G1, G2 and G3 (see 2.2.1, Fig. 1b) together with the calculated difference $\Delta\rho$ between the end measurement ρ_{end} and the pycnometry measurements ρ_{o-pyc} of unflooded material of same type (see Table 2).

In the NaCl flooded cores, $\Delta\rho$ ranged between –0.01 and +0.01 g/cm^3, except for two measurements (MO12, G1: +0.02 g/cm^3; AA21, G3: –0.02 g/cm^3). KA6, LI2 and AA21 saw a slight increase in P1 (+0.01 g/cm^3), while P2 in LI2 and AA21 stayed the same as unflooded material and P2 in KA6 decreased (–0.01 g/cm^3). The same trends were seen from the groups, although the absolute values were lower for AA21. The purest chalks MO12 and SK2 generally showed same density measurements as unflooded: for MO12 there was no response in P1 and P2, although the group measurements indicated an increase in G1 (+0.02 g/cm^3) and G3 (+0.01 g/cm^3) and no change in G2. SK2 displayed the same density as unflooded material in P1 with

an increase in P2 (+0.01 g/cm^3), while the group measurements indicated no density change along the core.

The solid density of the $MgCl_2$ flooded cores displayed a clearer trend towards increased density (compared to the NaCl flooded cores). The measurements of P1 and P2 varied from zero to +0.03 g/cm^3, and were higher in P1 than P2 for the cores KA8, MO10, LI2 and SK6, while in AA5 they were the same (P1, P2: +0.03 g/cm^3). The group measurements showed stronger variation, with $\Delta\rho$ varying from zero to +0.06 g/cm^3. Most noticeable, KA8 and SK6 had strong density peaks near the inlet ($\Delta\rho$ in G1: +0.06 g/cm^3 and +0.05 g/cm^3, respectively) and lower density towards outlet ($\Delta\rho$ in G3: +0.00 and +0.01 g/cm^3, respectively). MO10 showed increased density in G1 (+0.02 g/cm^3) and G3 (+0.01 g/cm^3), but no change in G2 (similar behaviour as MO12). LI1 gained its highest increase in G1 (+0.03 g/cm^3) and a somewhat lower increase (by +0.02 g/cm^3) in G2 and G3. AA5 displayed the same increase in G1 and G2 (+0.02 g/cm^3), but slightly lower increase in G3 (+0.01 g/cm^3).

Table 9 Solid density measured by pycnometry after flooding (ρ_{end}) for partitions P1, P2 and groups G1, G2, G3 (see Fig. 1b), and the difference ($\Delta\rho$) between measurement (ρ_{end}) of NaCl and $MgCl_2$ flooded cores and original solid density (Table 2, ρ_{o-pyc}). * no valid measurement was obtained for G1 in KA6.

NaCl flooded cores			$MgCl_2$ flooded cores		
	ρ_{end} (g/cm^3)				
P1	2.71	0.01	P1	2.73	0.03
P2	2.69	–0.01	P2	2.71	0.01
G1	*	*	G1	2.76	0.06
G2	2.69	–0.01	G2	2.71	0.01
G3	2.69	–0.01	G3	2.69	0.00
P1	2.70	0.00	P1	2.71	0.01
P2	2.70	0.00	P2	2.70	0.00
G1	2.72	0.02	G1	2.72	0.02
G2	2.70	0.00	G2	2.70	0.00
G3	2.71	0.01	G3	2.71	0.01
P1	2.70	0.01	P1	2.70	0.02
P2	2.69	0.00	P2	2.69	0.01
G1	2.70	0.01	G1	2.71	0.03
G2	2.70	0.01	G2	2.70	0.02
G3	2.69	0.00	G3	2.70	0.02
P1	2.68	0.01	P1	2.70	0.03
P2	2.67	0.00	P2	2.70	0.03
G1	2.67	0.00	G1	2.69	0.02
G2	2.67	0.00	G2	2.69	0.02

	G3	2.65	–0.02		G3	2.68	0.01
	P1	2.69	0.00		P1	2.71	0.02
	P2	2.70	0.01		P2	2.70	0.01
	G1	2.69	0.00		G1	2.74	0.05
	G2	2.69	0.00		G2	2.71	0.02
	G3	2.69	0.00		G3	2.70	0.01

3.10 Specific surface area (SSA)

Measurements of specific surface area (SSA_{end}) from slices 1, 3 and 7 of all flooded cores are listed in Table 10 together with the difference between these measurements taken from the flooded and unflooded material (Table 2).

The SSA in the NaCl flooded cores was either unchanged or reduced: The pure chalk cores SK2 and MO12 did not obtain any significant change compared to unflooded material. The more impure cores (KA6, LI2 and AA21) all saw a strong reduction (the average change varied from –0.5 to –1.3 m^2/g) towards values similar to the pure cores, ~ 2 m^2/g (Stevns Klint chalk, in Hjuler and Fabricius 2009). For LI2 the reduction (by –0.5 m^2/g, –0.4 m^2/g, –0.6 m^2/g along the core) was uniform, while for KA6 and AA21 the most significant reduction (–1.0 m^2/g and –2.8 m^2/g, respectively) was near the inlet.

In the $MgCl_2$ flooded cores the SSA increased strongly in all slices by 0.4 – 4.1 m^2/g, except for KA8 which saw a reduction in slices 3 and 7 and LI1 which had a small increase +0.1 m^2/g in slice 7 (Table 10**)**. The purest chalk SK6 had the same increase (by +1.0 m^2/g) in slices 1 and 3, with a smaller increase (+0.4 m^2/g) in slice 7, while MO10, KA8 and LI1 saw decreasing values along the core with the highest SSA near the inlet (MO10: 4.0 m^2/g; KA8: 3.5 m^2/g; LI1: 4.0 m^2/g;). I.e., for these cores the inlet SSA increased the most (MO10: +1.8 m^2/g; KA8: +0.5 m^2/g; LI1: +1.3 m^2/g) and the outlet SSA increased the least (MO10: +0.8 m^2/g; LI1: +0.1 m^2/g) or even decreased (KA8: –0.8 m^2/g). Unlike the other cores, the SSA increased along AA5 from inlet to outlet with values ranging from 6.7 to 9 m^2/g, higher than seen in any of the other $MgCl_2$ flooded core slices. The increase was also large compared to the other cores, ranging from 1.8 to 4.1 m^2/g.

Table 10 Specific surface area (SSA) of NaCl and $MgCl_2$ flooded cores. ΔSSA is the difference between the end measurement SSA_{end} and the measurement of SSA from unflooded material (Table 2).

NaCl flooded cores			$MgCl_2$ flooded cores		
	SSA_{end} (m^2/g)	ΔSSA (m^2/g)		SSA_{end} (m^2/g)	ΔSSA (m^2/g)

KA6	KA6–1	2.0	−1.0	KA8	KA8–1	3.5	0.5
	KA6–3	2.4	−0.6		KA8–3	2.4	−0.6
	KA6–7	2.6	−0.4		KA8–7	2.2	−0.8
	MO12–1	2.3	0.1		MO10–1	4.0	1.8
	MO12–3	2.2	0.0		MO10–3	3.6	1.4
	MO12–7	2.1	−0.1		MO10–7	3.0	0.8
	LI2–1	2.2	−0.5		LI1–1	4.0	1.3
	LI2–3	2.3	−0.4		LI1–3	3.5	0.8
	LI2–7	2.1	−0.6		LI1–7	2.8	0.1
	AA21–1	2.1	−2.8		AA5–1	6.7	1.8
	AA21–3	4.0	−0.9		AA5–3	7.8	2.9
	AA21–7	4.6	−0.3		AA5–7	9.0	4.1
	SK2–1	2.0	0.0		SK6–1	3.0	1.0
	SK2–3	1.9	−0.1		SK6–3	3.0	1.0
	SK2–7	1.9	−0.1		SK6–7	2.4	0.4

4 Discussion

4.1 Petrography, mineralogy, chemistry and isotope geochemistry

During flooding with NaCl there was minute dissolution of calcite (Fig. 8a) and Si–bearing minerals (AA21 and SK2, Fig. 8d) as detected by whole–rock geochemistry analyses, effluent analysis and FEG–SEM (Sup. Mat. Fig. 2). No new mineral precipitation was observed by XRD (Table 4, Sup. Mat. Fig. 5) or MLA (Table 5, Sup. Mat. Fig. 8a–c), which agrees with previous studies (Madland et al. 2011; Megawati et al. 2015). Only some crystals showed smoothened edges and corners in FEG–SEM studies.

In contrast, the cores that were flooded with $MgCl_2$ experienced strong geochemical alterations. Generally, during the $MgCl_2$ injection, dissolution of calcite and Si–bearing minerals and precipitation of Mg–bearing minerals took place (Fig 4c, Sup. Mat. Fig. 3, 6, 9). In all cores magnesite was detected by XRD and FEG–SEM images. This has also been observed and reported in the previous studies by Madland et al. (2011); Megawati et al. (2015); Zimmermann et al. (2013, 2015). MLA indicated formation of dolomite, but it was not verified by XRD. In all samples, increase of MgO and decrease of CaO could be observed in the geochemical

analysis, but the MgO enrichment varied between chalks (Table 6): The cores KA8 and AA5 gained more MgO than the other cores, starting from 0.2 wt% and 0.4 wt% and ending at average values of 2.3 wt% and 3.0 wt%, respectively. This change is supported qualitatively by XRD (3.2.3) and quantitatively by the effluent measurement (Fig. 8b, c) where the Mg^{2+}–ion concentrations in the effluent of KA8 and AA5 were lower than for the other cores (Fig. 8c). This corresponds to Mg^{2+} retention of 1.49 g in KA8 and 1.56 g in AA5. The other cores, SK6, MO10 and LI1 retained 1.29 g, 1.23 g and 0.93 g of Mg^{2+}, respectively. Both magnesite (3.0 g/cm^3) and Mg–rich calcite have higher density than calcite (2.71 g/cm^3), which was reflected in the measured increase of solid densities after flooding (Table 9). The SSA also increased due to the formation of nano–sized magnesite, Mg–rich calcite crystals and clay minerals, with smaller grain sizes than the former calcite crystals and because of the growth position on surfaces of the host mineral (Table 10, Sup. Mat. Fig. 3). The reactive variations between the chalk types may be attributed to differences in their depositional setting, original mineralogy and the consequently higher or lower intra–fossil porosity, more or less abundant fossil debris etc. As seen from MLA in Fig. 5c, mineral precipitation occurred to large extent in open pores spaces of microfossils.

The MgO content profiles along the cores also varied, with peaks at different locations. KA8 experienced the most changes in slice 1, from 0.2 wt% (unflooded sample) to 6.5 wt% (after flooding) and rapidly decreasing content towards the outlet slice (0.8 wt%). The cores MO10 and LI1 had peaks in MgO (2.5 wt% and 3.2 wt%, respectively) in slice 3 (not as strong as KA8), as confirmed by magnesite peaks in XRD. SK6 had a decreasing MgO content from slice 3 (2.9 wt%) to 7 (0.6 wt%) (data from slices 1 and 2 were not available). XRD and SEM–EDS indicated a peak in slice 2. Finally, AA5 indicated a high content of MgO in slice 2 (3.6 wt%), but with very uniform distribution with values of MgO content between 2.6 wt% and 3.6 wt% (also confirmed by SEM–EDS). This implies that the chalk type can affect the MgO distribution, most likely due to differences in primary non–carbonate content, thus the type and distribution of secondary phases, but also distribution of pores and microfossils. For comparison, in recent long–term tests on Liège chalk (Zimmermann et al. 2015) and related modelling results (Hiorth et al. 2013), most of the precipitated MgO accumulated near the inlet, with amounts decreasing rapidly towards the outlet.

Silica dissolution and re–precipitation (during $MgCl_2$ injection) as well as a significant concentration of Si^{4+} in the effluent could be observed in the chalk samples from Aalborg (Table

6**,** Fig. 8d). For the remaining chalks the changes in SiO_2 composition after testing was less significant with SiO_2 content after flooding close to original (Table 6).

On several occasions we saw that the analysis procedures had different detection limits. Most of the newly grown minerals had very small grain sizes, far below the spot size of the EDS of the FEG–SEM and the MLA. XRD can only detect a certain minimum amount of minerals and slices with several wt% MgO or SiO_2 did not always result in positive identification of Mg– or Si–bearing minerals by XRD. The limited change in C–O isotope values (Sup. Mat. Table 2) may also be explained by the relatively low net formation of new secondary minerals from the hot fluid, which would not change the isotope composition significantly. In longer lasting tests $\delta^{18}O_{SMOW}$ reflected the injection temperature when nearly the entire slice of a specific flooded chalk had been changed from calcite to magnesite (Zimmermann et al. 2013).

4.2 Significance of opal–CT in the Aalborg chalk cores

As seen, the Aalborg chalk stood out from the other types. A main characteristic is that Aalborg had both the most considerable fraction of SiO_2, and that it was in the form of opal–CT ($SiO_2 \cdot nH_2O$). In the other chalks the SiO_2 fraction was dominantly quartz, e.g. FEG–SEM images of unflooded material detected opal–CT in Aalborg (Fig. 3b, yellow square), but not in the other chalk types. The extraordinary shape of this crystal results in a high SSA (4.9 m2/g) compared to the rest (2–3 m2/g) and a low solid density (Table 2).

During flooding AA21 (~0.0012 mol/L) and AA5 (~0.0013 mol/L) displayed higher effluent concentrations of Si^{4+} than SK2 (~0.0007 mol/L) and SK6 (~0.0004 mol/L). Although such ICP–AES measurements were not made for the other cores, the whole–rock geochemistry indicated negligible alterations of the SiO_2 amount and spatial profiles apart from in the Aalborg cores (Table 6): AA21 displayed strong geochemical alteration after NaCl flooding (Table 6, Fig. 9a–c). The distribution of SiO_2 had a strong gradient from low values in slice 1 and 2 (2.4 wt%) to a plateau of more similar values (between 4.4 and 6.1 wt%) in slices 3 to 7. FEG–SEM images from AA21 after flooding could not detect opal–CT in slice 1 (Fig. 9a), but in slices 3 and 7 (Fig. 9b–c), corresponding to the locations where the SiO_2 content was low and high, respectively. The solid density changes (P1 (inlet): +0.01 g/cm^3, P2 (outlet): +0.00 g/cm^3) supports the dissolution of a lighter mineral phase in the near inlet region. Furthermore, the SSA (2.1 m^2/g) of AA21 in slice 1 after flooding (where the SiO_2 content was reduced from initially 4.9 to 2.4 wt%) is close to that of pure Stevns Klint chalk (1.7 m^2/g) (Hjuler and Fabricius 2009). The other chalk types saw no significant changes in SiO2 content or

distribution (but a trend in reduction of SSA towards pure chalk). It is natural to conclude both that opal–CT is reactive, much more so than quartz and that it was mainly opal–CT that dissolved in AA21. Also, the SiO_2 profile combined with the locations of observed opal–CT grains (only in slices towards the outlet), suggest that the dissolution process occurs very fast, i.e. the brine becomes saturated (and less reactive) towards this mineral just after very short time in the core.

After flooding, our findings suggest that the reactive presence of opal–CT in Aalborg chalk plays a crucial role. The high Si^{4+} concentration obtained by dissolution of opal–CT allows interaction with Mg^{2+} in the brine, resulting in re–precipitation of new minerals, see FEG–SEM images of slice 1, 3 and 7 of AA5 in Fig. 9d–f. It is possible that talc was part of the new phase as indicated by MLA only for this core, but it was not verified by XRD. The formation of these new minerals (along with other Mg–bearing minerals) resulted in increased SSA. Particularly, the SSA (4.99 m^2/g in unflooded material, Table 2) increased towards the outlet, in range 7 to 9 m^2/g, consistent with the distribution of SiO_2 and the slices where the newly formed Si–Mg–bearing minerals were detected. The other $MgCl_2$ flooded cores (KA8, MO10, LI1, SK6), which did not indicate formation of such minerals did not obtain higher SSA than 4 m^2/g.

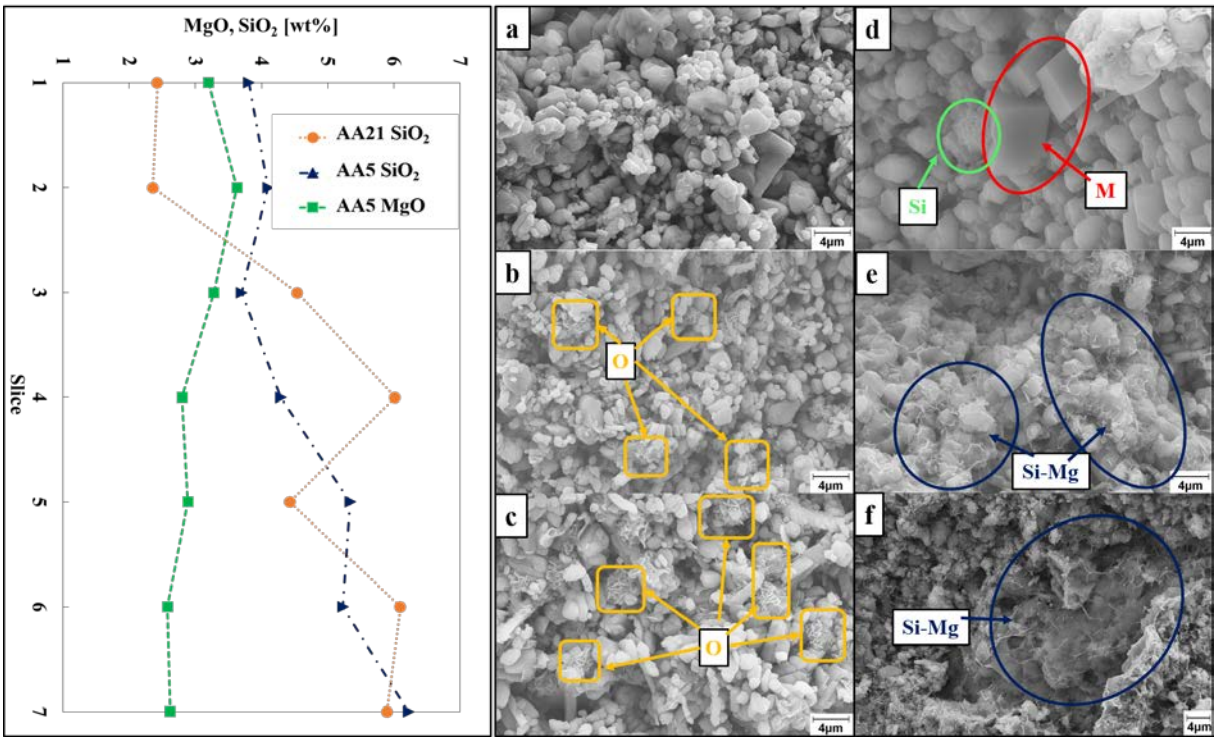

Fig. 9 The distribution (wt%) of SiO_2 and MgO along the core (left) are shown, along with FEG–SEM images from AA5 and AA21 (right): (a) AA21–1 (inlet), (b) AA21–3, (c) AA21–7 (outlet) and (d) AA5–1 (inlet), (e) AA5–3, and (f) AA5–7 (outlet). In AA5–1 we observe Si–bearing minerals (green circle) formed on top of a newly formed magnesite crystal (red circle).'M': Magnesite was observed; 'Si–Mg': Si–Mg–bearing mineral was found in slices AA5–3 and AA5–7 as a thin coating (blue

circles). The inlet slices AA5–1 and AA21–1 both display rounded grains indicative of dissolution. 'O': Opal–CT (yellow square) was detected in slices AA21–3 and AA21–7, but not in the inlet slice AA21–1. The SiO_2 content had been much reduced in the first two slices of this core.

4.3 Modelling with PHREEQC

Flooding experiments of Aalborg chalk, including NaCl brine (AA21) and $MgCl_2$ brine (AA5) were replicated in a 1D advection dispersion reaction (ADR) model set up in PHREEQC v3 (Parkhurst and Appelo 2013), a geochemical software. Similar modelling of core flooding tests considering more complex brines into pure chalk were performed in Madland et al. (2011); Andersen et al. (2012), while modelling of $MgCl_2$ injection in a fracture–matrix context was considered by Andersen and Evje (2016). The current analysis was performed in order to investigate the role of Si^{4+}–ions in the physicochemical interplay in light of the experimental observations.

Variables of minerals, brine ions and surface ions are represented by concentrations C_i given in mol per L pore volume. As initial rock composition we apply the average composition of Aalborg chalk given in Table 6a, assuming SiO_2 belongs to opal–CT and MgO to magnesite, while the rest is calcite. A porosity of $\varphi = 47\ \%$ (see Table 2) was assumed. Opal–CT consists of cristobalite and tridymite; for simplicity the properties of cristobalite were taken as representative (Table 11). The conversion from mineral mass fraction p_i to mineral concentration C_i was made as follows:

$$C_i = \frac{\frac{p_i}{MW_i}}{\sum_{j:minerals}\frac{p_j}{\rho_j}}\frac{(1-\varphi)}{\varphi}, \tag{4}$$

where MW_i is mineral molar weight and ρ_i is mineral density (see values in Table 11). The initial brine is DW equilibrated with calcite and opal–CT. The injected brine is either 0.657 mol/L NaCl or 0.219 mol/L $MgCl_2$ with carbon concentration corresponding to what dissolves at atmospheric conditions ($P_{co2} = 10^{-3.5}$ atm); roughly $1.3 \cdot 10^{-5}$ mol/L. The core is 7 cm in length, the injection rate 1 PV/d and the temperature 130 °C. 35 grid cells were used. Equilibrium calculations predicted that opal–CT and calcite could dissolve in NaCl brine and that re–precipitation of quartz could occur. As newly formed quartz could not be detected or significantly improve the modelling it was not included. Further, $MgCl_2$ saturated with calcite and opal–CT could precipitate several Mg– or Si–bearing minerals such as brucite, dolomite, monticellite, quartz and talc. As magnesite and talc were indicated from the geological analysis they were included in the model, in addition to calcite and opal–CT.

We include mineral dissolution and precipitation reactions (see Table 11) using kinetic rates of the following form (Palandri and Kharaka 2004; Appelo and Postma 2005):

$$\frac{dc_i}{dt} = -RF_i \left(\frac{A}{V}\right)\left(\frac{m}{m_0}\right)^{r_i} (k_{1,i} + k_{2,i} a_h^{n_i}) \operatorname{sign}(1-\Omega)\,|1-\Omega_i^{p_i}|^{q_i}, \qquad (5)$$

for the minerals i = calcite, magnesite, opal–CT and talc, where $\Omega_i = \frac{IAP_i}{K_i}$ represents the saturation state (ratio of the ion activity product IAP_i and solubility constant K_i) for each mineral. I.e., if a mineral is oversaturated it precipitates, while if it is under–saturated (and its concentration is positive) it dissolves. $\left(\frac{A}{V}\right) = 14580$ m^2/L represents the original ratio of surface area to fluid volume based on average parameters from the two Aalborg cores. The factor $\left(\frac{m}{m_0}\right)^{r_i}$ is the ratio of current and initial moles, representing reduction in available surface area for a dissolving mineral. This factor was only used for opal–CT with $r_i = \frac{2}{3}$. a_h is the activity of H^+, while $k_{1,i}$, $k_{2,i}$, p_i, q_i are mineral and/or temperature specific parameters collected from Palandri and Kharaka (2004). The reference assumption was that the full surface area of the rock was available for precipitation and dissolution, while a reduction factor $RF_i < 1$ was included to account for less available area. Ion exchange of Na^+, Ca^{2+} and Mg^{2+} was included to capture the early Ca^{2+} peak and delay of Mg^{2+} observed in the effluent profiles (Fig. 6a,b). For treatment of charge balance, carbon speciation, complexes, etc. we refer to Parkhurst and Appelo (2013); Appelo and Postma (2005); Andersen et al. (2012).

The four reaction rate coefficients RF_i and three ion exchange parameters (cation exchange capacity and two equilibrium constants, see Andersen et al. (2012)) were tuned in order to match the effluent time profiles and geochemistry spatial profiles after flooding. The parameters were uniquely matched and applied with same values in both the NaCl and $MgCl_2$ tests; AA21 and AA5. It was necessary to reduce the rates significantly varying from a factor of RF=0.08 (for opal–CT) to 10^{-9} for talc (see Table 11). For opal–CT the RF was very close to the initial content (5.6 wt%). It is possible that the great oversaturation of talc and magnesite at high temperature and the fact that they were precipitating and not dissolving exceeded the validity of the literature rates, hence the need to reduce their magnitude. It is also possible that the available area for precipitation is less than the full surface area of the rock.

Table 11 Parameters used in simulation. *Solid species (s) on left side, aqueous species on right side. **For opal–CT the density and solubility of cristobalite is assumed, along with a molar weight based on 10 % hydration. Notation: K_i – solubility constant, ρ_i – mineral density, p_i – mineral weight fraction, C_i – mineral concentration, RF_i – rate reduction factor.

Mineral i	Dissolution reaction*	$\log K_i$ at 130 °C (–)	ρ_i (g/cm^3)	MW_i (g/mol)	Initial p_i (–)	Initial C_i (mol/L)	RF_i (–)
Calcite	$CaCO_3\ (s) \leftrightarrow\ Ca^{2+} + CO_3^{2-}$	0.39	2.71	100.09	0.935	28.09	4.75e–7
Magnesite	$MgCO_3\ (s) \leftrightarrow\ Mg^{2+} + CO_3^{2-}$	0.04	3.10	84.31	0.009	0.32	1.43e–4
Opal–CT**	$SiO_2 \cdot nH_2O\ () \leftrightarrow\ SiO_2 + nH_2O$	–2.46	2.33	66.76	0.056	2.53	8e–2
Talc	$Mg_3Si_4O_{10}(OH)_2(s) \leftrightarrow\ -6\ H^+ + 3\ Mg^{2+} + 4\ H_2O + 4\ SiO_2$	13.27	2.71	379.27	0.000	0	1.0e–9

4.3.1 *NaCl flooding tests*

There was a discrepancy between the measured changes in SiO_2 composition (Table 6b) and the measured effluent Si^{4+} concentration (~0.001 mol/L, see Fig. 8d) from AA21. It was assumed that the geochemistry measurements were more accurate as they are cumulative, and some mismatch of the Si^{4+} effluent concentration was accepted (Fig. 6a). The amount of dissolved SiO_2 and the spatial profile were then well matched (Fig. 6b) using the literature rate (normalized to initial content). The observed SiO_2 wt% profile can be explained by rapid dissolution of opal–CT: the brine gets saturated after 3 – 4 cm with little dissolution downstream. Matching towards the effluent would give less dissolution and a more uniform profile.

The literature rate of calcite dissolution was sufficiently high to achieve full saturation ($\Omega_{calcite} = 1$) after flooding. Any tuning of $RF_{calcite}$ maintained this property. The predicted effluent Ca^{2+} concentration was 0.00092 mol/L at steady state. That is roughly a factor of 4 lower than measured values, but within the range of uncertainty (the measurements were near or below the detection limit, see Sup. Mat. 1.7). Ca–Si–complexes were evaluated to have negligible effect on the dissolution process, contrary to the statements in Fabricius and Borre (2007); the predicted production of Ca^{2+} was the same (~1 % difference) whether Si^{4+} was present in the system or not (reasonable for SK2 and MO12). On the other hand, much of the Si^{4+}–ions were bound in complexes with Na^+, effectively increasing the solubility by ~15 % compared to DW (seen by the increasing Si^{4+} concentration the first PVs in Fig. 6a). Ion exchange parameters of Na^+ and Ca^{2+} were tuned to give a peak 2 – 3 times higher than the steady state level.

Mass rates $\frac{dM}{dt}$ [g/mol] were calculated based on the injected and effluent concentrations C_i [mol/L] of the aqueous species, using their molar weight (g/mol) and injection rate Q [L/d] (see Table 2) as follows:

$$\frac{dM}{dt} = Q \sum_{i:aq} \left(C_i^{inj} - C_i^{eff}\right) MW_i. \quad (6)$$

First, only considering the production of Ca^{2+} and CO_3^{2-} (assuming non–reactive Si^{4+}) we obtain a mass rate of –0.0033 g/d, which is in the range of mass rate for the pure cores MO12 (–0.010 g/d) and SK2 (–0.002 g/d), but also the impure chalks with quartz; KA6 (–0.008 g/d) and LI2 (–0.006 g/d), see also Table 7. Adding the contribution from predicted SiO_2 (aq) production (effluent concentration 0.0044 mol/L) we obtain a mass rate of –0.013 g/d which is larger than the mentioned cores and more close to the measured mass rate of AA21 (–0.025 g/d). For this case the production of SiO_2 accounts for 74 % of the mass loss.

4.3.2 *$MgCl_2$ flooding tests*

Also for the core AA5 there was a discrepancy between the effluent measurements of Si^{4+} and the whole–rock geochemistry for SiO_2: 1) The effluent Si^{4+} measurements (0.0013 mol/L) were ~ 2.5 times lower than the production required (0.0032 mol/L) to produce the measured changes in SiO_2 (as for AA21). Also, 2) the effluent measurements suggested a higher production of SiO_2 from AA5 (MgCl2) than AA21 (NaCl), see Fig. 6d. On the other hand the geochemistry measurements suggested a greater loss of SiO_2 from AA21 ($MgCl_2$) than AA5 (NaCl). The model predicts that even without precipitation of secondary minerals, $MgCl_2$ dissolves less opal–CT than NaCl, further supporting to match the geochemistry also for this test.

The dissolution of calcite and precipitation of magnesite are closely coupled and is more or less a substitution process on core scale for wide ranges of their rate parameters (the mass is however reduced since Mg weighs less than Ca). Increasing the magnitude of either calcite or magnesite reaction rates led to more substitution (more production of Ca^{2+} and retention of Mg^{2+}), while altering the ratio of the two rates while keeping a fixed production affected the magnesite precipitation profile in the core. The dissolution rate of opal–CT was kept from the simulation of AA21. The predicted dissolution of opal–CT then resulted in higher Si^{4+} production than indicated by the geochemical changes of SiO_2 (Table 6) suggesting significant re–precipitation of Si–bearing minerals in the core, and the difference was eliminated by tuning the reaction rate of talc. Further, precipitation of talc affected the produced sum of Ca^{2+} and Mg^{2+} (i.e. making it no longer a substitution). These measurements were thus also an indirect observation of the extent of talc precipitation.

The effluent profiles of Ca^{2+} and Mg^{2+} were matched, see Fig. 10c, where the early transient phase was modelled by ion exchange of Ca^{2+} and Mg^{2+}. The simulated time frame of the ion exchange period was limited to the first ~15 PV, while transient effects were seen until ~25 PV.

This could be better captured by a time–dependent increase of ion exchange capacity: as observed in Table 10, the SSA increased significantly during the AA5 test. A closer view of the low concentration effluent profiles is seen in Fig. 10d, especially comparing the predicted and measured Si^{4+} effluent profiles. The order of magnitude is well captured. Measured spatial profiles of MgO and SiO_2 describe quantitatively the local amount of an element in the rock, but not how it is distributed into different minerals. It was therefore decided to tune the model such that the total contribution of different species matched those measurements. The result is given in Fig. 10e for Mg^{2+}–species with a good match of both magnitude (indicative of consistency with effluent measurements) and spatial profile. Notably, magnesite is distributed evenly except for low concentrations at the inlet. A magnesite peak is given between 2 and 3 cm from the inlet, which is consistent with the XRD measurements, indicating a magnesite peak in slices 2 and 3 (Fig. 4c). Some Mg^{2+} is retained to the surface by adsorption with higher concentrations near the inlet (where the Mg^{2+}/Ca^{2+} concentration ratio is higher). Talc is predicted to be distributed along the entire core, in agreement with the MLA (Table 5). The simulated talc profile was however not in complete accordance with experimental measurements which indicated increasing amounts of talc towards the outlet (Fig. 9d, e, f), while the simulations indicated the opposite trend. As talc was not positively verified by XRD (Fig. 4c) (merely indicated by MLA, see Fig. 5c and Table 5), other geologically relevant Si–Mg–minerals, such as monticellite $CaMgSiO_4$, were simulated, but also yielding same trend, decreasing in concentration from the inlet towards the outlet. This mismatch indicates that some mechanisms are yet not accounted for in the model. We note that changes in permeability, porosity, surface area could be such factors, but also solids transport or a more complex precipitation mechanism than applied here. The calculated and measured spatial Si–profiles after flooding AA5 are given in Fig. 10f, again displaying good agreement between the SiO_2 measurements and the total Si concentration profile. Opal–CT was heterogeneously distributed in unflooded Aalborg chalk (ranging between 4 and 6 wt% SiO_2, see Table 6a or Sup. Mat. Table 1), which can explain some of the variations along the core. A noticeable fraction of the initial opal–CT has been dissolved and converted into talc. The re–precipitation effect has led to a higher degree of opal–CT dissolution as seen by comparing Fig. 10f with Fig. 10b (NaCl flooded AA21). Opal–CT has been significantly dissolved along the entire core in the case of AA5, unlike AA21 where only half the core was affected. We further note that the precipitation mechanism of talc induced a higher dissolution of calcite: The predicted steady state effluent Ca^{2+} concentration from AA5 when setting the talc and opal–CT reaction rates to zero (only calcite and magnesite minerals accounted for) was 0.006 mol/L lower (originally 0.025 mol/L,

see Fig. 10d). As expected, the measured average MgO content in AA5 (3.00 wt%) was the highest of all the cores, see Table 6c, while the originally pure cores MO10 and SK6 obtained the lowest values (1.49 and 1.54 wt%, respectively). Similarly, AA5 (–4.15 g) had the highest mass loss, while MO10 (–1.57 g) and SK6 (–1.11 g) lost the least mass, see Table 7. The high dissolution of calcite corresponds well the high compaction of AA5 and AA1, seen in Fig. 7b, compared to the other cores.

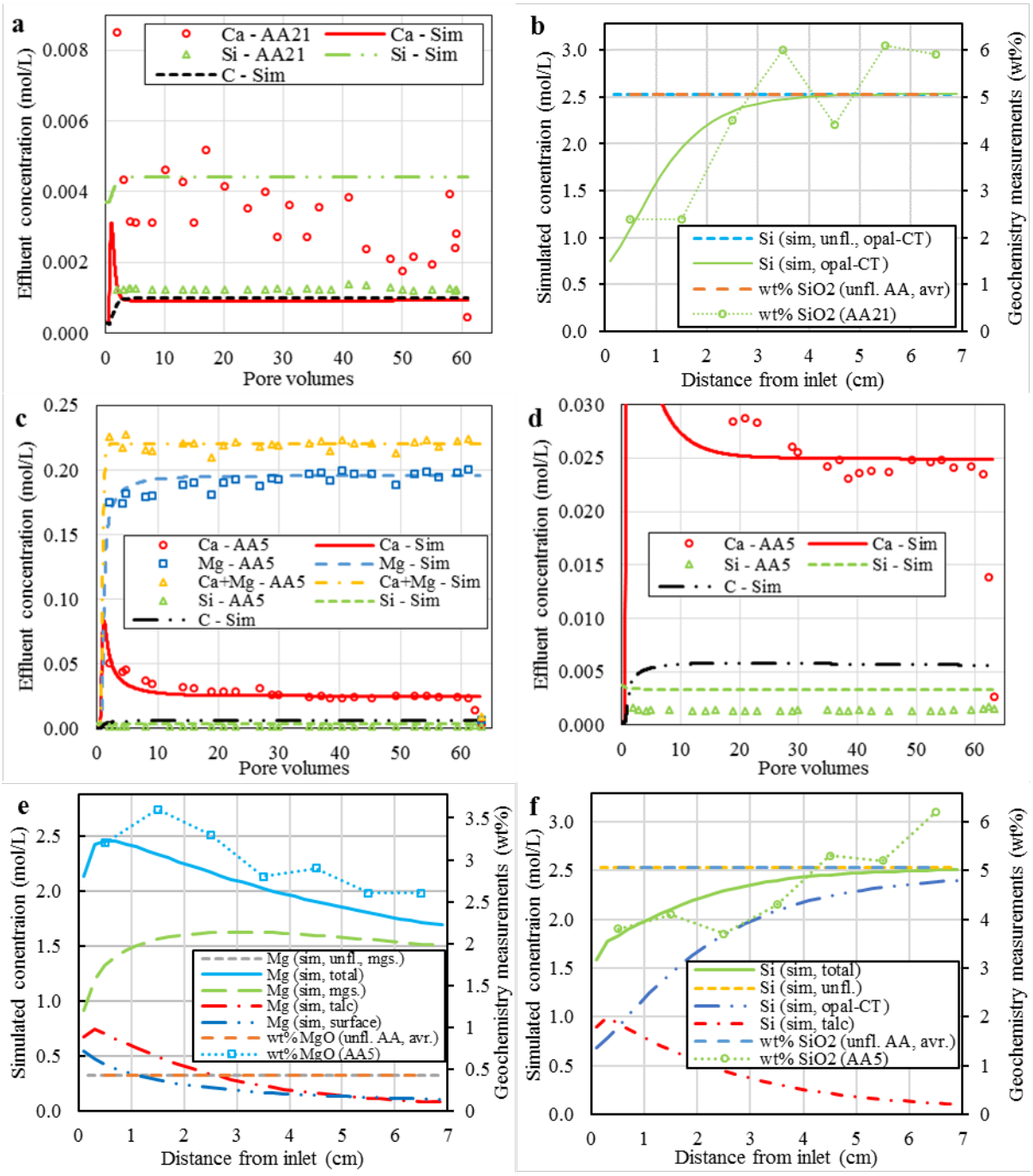

Fig. 10 Simulation (Sim) results from PHREEQC compared with experimental data (marked by core name). (a): effluent from AA21; (b): spatial Si–profiles from AA21; (c): effluent from AA5; (d): effluent from AA5 with focus on small concentrations; (e): spatial Mg–profiles from AA5; (f): spatial Si–profiles from AA5. Initial composition (unfl.) is based on average

composition of unflooded Aalborg (unfl. AA, avr.). Concentration variables are scaled to match wt% measurements initially. All variables given in mol/L (left axis) unless specified to wt% (right axis). Simulated element contribution from different minerals is indicated.

4.4 Compaction and chemistry

As presented, NaCl flooding is typically performed to produce baseline results from which one can reduce or eliminate the impact of chemical effects. Considering the creep compaction profiles in Fig. 7a, we note that cores with higher content of SiO_2, experienced less deformation. Apparently, Si–bearing minerals can add to the strength of chalk during the creep phase. The most impure cores AA21 and LI2 produced the most Ca^{2+} among these cores (on average 0.0036 and 0.004 mol/L, respectively) (Fig. 8a), but of such a small amount (near the detection limit) that it likely did not impact the weakening of the chalk. In SK2 the production of Si^{4+} was also very low (~0.0007 mol/L). AA21 saw a more significant dissolution (0.0012 mol/L) in SiO_2 content (Fig. 8d, Table 6), but still contained after flooding higher SiO_2 content than the other chalk cores, and compacted the least.

For the $MgCl_2$ flooded cores the trend was opposite. The two most impure cores AA5 and AA1 clearly compacted the most (AA5: 5.47 %, AA1: 6.55 %, Fig. 7b). The other cores showed less, but roughly similar compaction (KA8: 2.99 %; MO10: 3.2 %; LI1: 3.57 %; SK6: 3.58 %; SK1: 3.22 %). SK1, SK6, MO10, and LI1 showed creep acceleration (Fig. 7b). In particular, for the pure chalks SK1, SK6 and MO10 a delay period of low compaction rate was observed, followed by creep acceleration and higher compaction rate. KA8 saw a slight increase in compaction rate (up to 40 days), while LI1 saw a more clear, but gradual transition from slow (5 – 22 days with creep strain from 1.41 to 1.57 %) to faster compaction (~ 23 days with creep strain 1.75 %). From the performed tests we note that if acceleration happened at later times it also occurred at higher strain (see Fig. 7b, Table 12). Considering the chalk types, these parameters mostly increase with amount of non–carbonates (mainly SiO_2), although KA8 breaks this trend, showing a slight compaction rate increase at an early time, but its low original porosity may be a factor. Although there could be a correlation between the onset of creep acceleration and chalk impurity, reliable prediction requires a more fundamental understanding.

Table 12 Data for cores, which exhibited creep acceleration: SiO_2 (wt%), time of acceleration and axial strain in delay period.

Core	SiO_2 (wt%)	Onset of creep acceleration (d)	Strain in delay phase (%)
SK1	0.35	7	0.3
SK6	0.33	15	0.5

MO10	0.92	26	0.8
KA8	1.7	9	0.4
LI1	2.2	32	1.5

The compaction behavior was also reflected in the effluent concentration profiles. The cores having continuous compaction development (AA5 and KA8) also produced a monotonously decreasing effluent Ca^{2+} concentration before stabilizing, see Fig. 8b. The pure chalk cores MO10 and SK6 and the more impure core LI1, which experienced creep delay and accelerated creep, produced decreasing Ca^{2+} effluent concentrations to a minimum value (MO10: 0.018 mol/L; LI1: 0.015 mol/L; SK6: 0.013 mol/L). Then, roughly at the time of creep acceleration, the Ca^{2+} production increased significantly and reached a stable state (MO10: 0.024 mol/L; LI1: 0.018 mol/L; SK6: 0.022 mol/L). Accordingly, the Mg^{2+} effluent concentration obtained peaks before stabilizing, see Fig. 8c. These observations indicate once more the coupled nature of chemistry and compaction, by displaying increased chemical interaction at higher compaction rates. Comparing with previous studies (Madland et al. 2011) a Liége core injected with $MgCl_2$ at same conditions displayed continuous compaction (like the Aalborg cores), i.e. no delay phase or acceleration, and the effluent Ca^{2+} profile was monotonously decreasing. In addition, also common with the Aalborg cores, significant concentrations of Si^{4+} were detected in the effluent (~0.0025 mol/L) and re–precipitation of Si–bearing mineral was observed. These common features seen for two different chalk types (Liége and Aalborg) could suggest that an active Si–chemistry affects both mineralogical alterations, effluent profiles of the divalent ions and the compaction behaviour.

To see the effect of brines on compaction, the axial creep strain of the $MgCl_2$ flooded cores (ε_{MgCl2}) is plotted *versus* the axial creep strain of the NaCl flooded cores (ε_{NaCl}) of the same chalk type in Fig. 11. For data following $\varepsilon_{MgCl2} = \varepsilon_{NaCl}$ (dotted line in Fig. 11) there are no significant effects from the rock–brine chemistry. Most of the chalk types followed this trend initially, but deviated more for creep strains > 0.5 %. Considering Fig. 7 this corresponds to 1 – 5 injected PVs, indicating brine sensitivity very early. The purest chalk cores MO10, SK1, SK6 and KA8 at first experienced less deformation with $MgCl_2$ than their corresponding cores MO12, SK2 and KA6 injected with NaCl brine, for $\varepsilon_{NaCl} < 1.5$ %. The ratio between the strains, $\varepsilon_{MgCl2} / \varepsilon_{NaCl}$, did not reach below 0.5. The two LI cores compacted with similar magnitude for strains < 1.8 %. In long term, however, all these chalks eventually obtained more deformation with $MgCl_2$ than with NaCl (the ratio $\varepsilon_{MgCl2} / \varepsilon_{NaCl}$ stayed below 2 during the test period). For Aalborg, the chalk with highest non–carbonate content, this effect was observed from the start:

AA5 and AA1 ($MgCl_2$ flooded) both displayed consistently higher strains than for AA21, and the difference increased gradually with time.

The mineralogical processes initiated by Mg^{2+} seem to inhibit compaction in pure chalk types (MO, SK and KA) compared to NaCl during the initial creep phase, but in the long run the compaction will be more significant, regardless of chalk type. Also Zhang et al. (2011) observed that $MgCl_2$ can inhibit creep compaction compared to NaCl in milled limestone (> 99 wt% calcite) at 150 °C. In this study we could also observe acceleration in creep following the mentioned delay / inhibition period (Fig. 7).

The impact brines had on compaction, is represented in Fig. 11 and corresponds well with the mineralogical changes. As seen in Zimmermann et al. (2013), it is assumed that dissolution of the chalk matrix, triggered by the non–equilibrium fluids, can enhance the precipitation of Mg–bearing minerals. The extent of increased compaction (compared with NaCl flooding) correlated well with the amount of MgO in the cores after flooding (KA8: 2.3 wt%; AA5: 3.0 wt%; SK6: 1.5 wt%; MO10: 1.5 wt%; LI1: 1.8 wt%, the cores had similar initial content of MgO, 0.2 – 0.4 wt%, Table 6). As exception, KA8 obtained a high MgO content and low compaction, but it is likely related to its lower porosity.

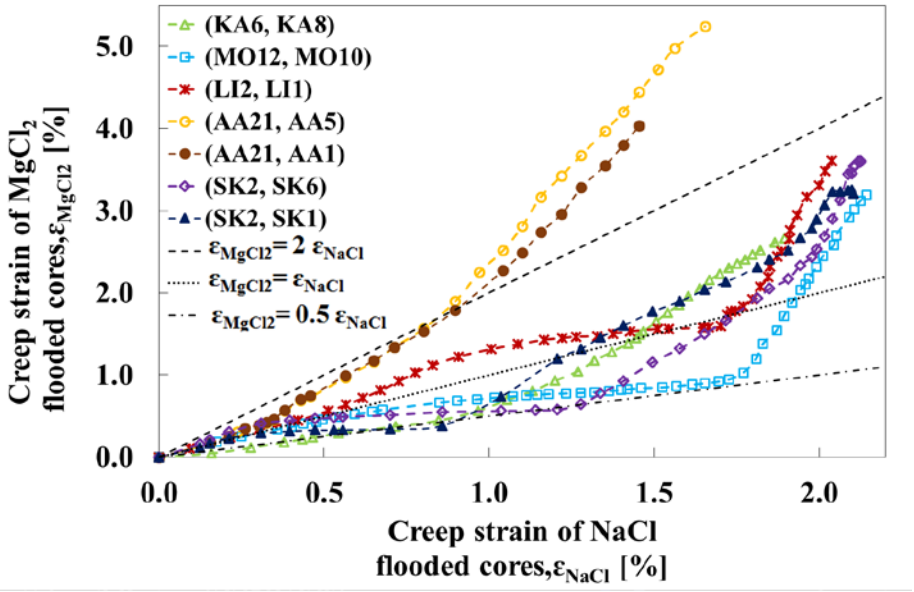

Fig. 11 Axial creep strain comparison between $MgCl_2$ and NaCl flooded cores. The strain data ε_{MgCl2} of each $MgCl_2$ flooded core is plotted vs. the strain ε_{NaCl} of the NaCl flooded core of same chalk type. The graph label reads '(NaCl flooded core, $MgCl_2$ flooded core)'. Lines indicating equal, half (0.5) and double (2) deformation with $MgCl_2$, compared to NaCl, are indicated.

4.5 Application of the results

In recent years ‘smart water’ brines, which typically involve modifying the natural setup of ions in seawater (Ca^{2+}, Mg^{2+}, SO_4^{2-}, Na^{+}, Cl^{-}), have been more and more investigated to increase oil recovery by attempting to change wettability, avoid scaling, but also predicting or controlling the extent of compaction. Our work, together with the Si–bearing minerals finding by (Madland et al. 2011), demonstrates that the original mineralogy, especially the non–carbonate content, the newly formed minerals caused by dissolution and formation of secondary minerals in addition to re–precipitation of new minerals, can control the chemo–mechanical interactions and should be taken into account when predicting reservoir behavior from laboratory studies (i.e. the Ekofisk field contains considerable amounts of non–carbonate minerals (Van den Bark and Thomas 1981)).

Chalk–fluid interactions at field scale is still a great challenge. In particular, fractured reservoirs in the North Sea have high porosity (up to 45 %), low matrix permeability (3 – 4 mD) and small matrix block size. In order to understand the complex mechanisms and dynamics a mathematical interpretation of the geochemical interaction was performed, capturing the main trends and observations. Taking the results to predicting performance during brine injection at field scale, the systematic laboratory analysis of chalk–brine interactions in this study can be helpful in bridging the gap when it comes to the effect of non–carbonate mineralogy in chalk. Potentially the results can be used for predicting the extent of mineralogical changes and transformation of reservoir properties in fracture and matrix, e.g. our measurements show that the mineralogical alterations significantly affected the specific surface area, which is an indicator of permeability in chalks (Hjuler and Fabricius 2009; Megawati et al. 2015). The experimental results presented in this paper were made at a constant high temperature (130 °C representative of Ekofisk conditions). Both multiphase flow properties and reaction kinetics are strongly temperature dependent. In a producing field, cold water is normally injected, and thus temperature–dependent reaction kinetics and compaction models should be developed or predicted and up–scaled before industrial application.

5 Conclusions

This study has considered five types of outcrop chalks (Kansas, Mons (Triviéres Fm.), Liège, Aalborg and Stevns Klint, sorted from old to young), with similar age and high porosity, exposed to identical core flooding–compaction tests at 130 °C in creep state. Dual tests were performed where chalk cores were injected with 0.219 mol/L $MgCl_2$ or 0.657 mol/L NaCl at 1

PV/d over a period of 2 – 3 months to simulate reservoir conditions of some hydrocarbon reservoirs in the North Sea.

In this study, extensive analysis of unflooded and flooded material were made to systematically interpret mineralogical and chemical changes along the core samples (sliced in seven equal slabs) by means of XRD, SEM–MLA, SEM–EDS, whole–rock geochemistry, stable isotope geochemistry and BET (N_2). These methods are sensitive to alterations of the core and showed that non–carbonate chemistry (mainly Si–bearing minerals) does affect rock mechanical parameter and processes. The diagenetic variations may help in establishing useful guidelines in searching for the best substitute analogous to the North Sea reservoir chalk with respect to mechanical and mineralogical properties. The measurements were also interpreted by mathematical modelling supporting the interpretation of the mechanisms in the Aalborg chalk: opal–CT dissolves very reactively both with NaCl and $MgCl_2$ brines. The released Si^{4+}–ions can interact with injected Mg^{2+}– and Ca^{2+}– ions and re–precipitate as new mineral phases such as talc, consistent with experimental observations. The formation of these new minerals can trigger enhanced dissolution of calcite, which can explain the high compaction rate seen in the Aalborg cores (Fig. 7b) flooded with $MgCl_2$.

Mg–bearing minerals, mainly magnesite and Mg–rich calcite are precipitated in the $MgCl_2$ flooded cores (KA8, MO10, LI1, AA5, and SK6). The cores KA8 and AA5 obtained more retention of Mg^{2+} than other cores (MO10, LI1, and SK6) in the geochemical measurement, which is also supported by the effluent analysis. This is reflected in the measured increased solid densities and increased SSA. The MgO distributions along the cores behave differently. The sample KA8 obtained the MgO peak near the inlet, while in AA5 a uniform pattern was observed. In the other three chalk types the highest values occurred near the centre along the flooding direction of the cores. This implies that the MgO precipitation is not only time dependent, but also chalk type dependent, hence influenced by the genesis of the rock. In addition, Aalborg chalk contained abundant opal–CT, which was significantly dissolved with both NaCl and $MgCl_2$ brines. Si–Mg–bearing minerals (interpreted as talc by MLA) was detected as newly grown phase in $MgCl_2$ flooded Aalborg chalk and could be related to a significantly increased specific surface area. The other chalks, where SiO_2 was bound mainly in quartz, did not see strong alterations in SiO_2 distribution after flooding. These findings suggest opal–CT plays an important role.

In creep phase, NaCl flooded cores with higher SiO_2 content compacted less, while cores exposed to $MgCl_2$ compacted more with increasing SiO_2 content. The cores flooded with $MgCl_2$

compacted more than that with NaCl given sufficient time, however for a period $MgCl_2$ inhibited compaction in pure chalks compared to NaCl.

The study concludes that precipitation of new minerals not originally present, triggering enhanced matrix dissolution of original minerals is the key driving force for chemical creep compaction in these core flooding experiments. In future studies we plan to assess the contribution of mechanisms and parameters such as pressure solution, porosity and creep stress which in this study are considered less important.

Acknowledgements

The authors thank the Faculty of Science and Technology for the PhD grant for W. Wang. Thanks for the SEM work (AA5) done by Tania Hildebrand–Habel. The authors thank COREC for financial support for this research study and acknowledge the Research Council of Norway and the industry partners; ConocoPhillips Skandinavia AS, BP Norge AS, Det Norske Oljeselskap AS, Eni Norge AS, Maersk Oil Norway AS, DONG Energy A/S, Denmark, Statoil Petroleum AS, ENGIE E&P NORGE AS, Lundin Norway AS, Halliburton AS, Schlumberger Norge AS, Wintershall Norge AS of The National IOR Centre of Norway for support. The research presented is integral part of the PhD thesis of W. Wang at UiS.

References

Anderson, T. F., Arthur, M. A.: Stable isotopes of oxygen and carbon and their application to sedimentologic and environmental problems. In: Arthur, M.A., Anderson, T. F., Kaplan, I.R., Veizer, J., Land, L. S. (eds.) Stable Isotopes in Sedimentary Geology. Society of Economic Paleontologists and Mineralogists, Short Course Notes. **10**, 1–151 (1983). doi:10.2110/scn.83.01.0000

Andersen, P. Ø., Evje, S., Madland, M. V., Hiorth, A.: A geochemical model for interpretation of chalk core flooding experiments. Chem. Eng. Sci. **84**, 218–241 (2012). doi: 10.1016/j.ces.2012.08.038

Andersen, P. Ø., Evje. S: A model for reactive flow in fractured porous media. Chem. Eng. Sci. **145**, 196–213 (2016). doi:10.1016/j.ces.2016.02.008

Appelo, C. A. J., Postma, D.: Geochemistry, groundwater and pollution. Boca Raton, Fl, Taylor & Francis Group (2005)

Bertolino, S.A.R., Zimmermann, U., Madland, M.V., Hildebrand–Habel, T., Hiorth, A., Korsnes, R.I.: Mineralogy, geochemistry and isotope geochemistry to reveal fluid flow

process in flooded chalk under long term test conditions for EOR purposes. In: XV International Clay Conference, Brasil. 676 (2013)

Bjørlykke, K., Høeg, K.: Effects of burial diagenesis on stresses, compaction and fluid flow in sedimentary basins. Mar. Petrol. Geol. **14**, 267–276 (1997). doi:10.1016/s0264-8172(96)00051-7

Bjørlykke, K.: Relationships between depositional environments, burial history and rock properties. Some principal aspects of diagenetic process in sedimentary basins. Sediment. Geol. **301**, 1–14 (2014). doi:10.1016/j.sedgeo.2013.12.002

Brindley, G. W., Brown, G.: Crystal structure of clay minerals and their X–ray identification, in: Brindley, G. W., Brown, G. (eds.). Mineralogical society monograph. **5**, 361–410 (1980)

Collin, F., Cui, Y. J., Schroeder, C., Charlier, R.: Mechanical behaviour of Lixhe chalk partly saturated by oil and water: experiment and modelling. Int. J. Numer. Anal. Met. **26**, 897–924 (2002). doi: 10.1002/nag.229

Engstrøm, F: Rock mechanical properties of Danish North Sea chalk. Proceedings of 4th North Sea Chalk Sym, Deauville (1992).

Fabricius, I. L.: Compaction of microfossil and clay–rich chalk sediments. Phys. Chem. Earth. Pt. A. **26**, 59–62 (2001). doi:10.1016/S1464-1895(01)00023-0

Fabricius, I. L.: Chalk: composition, diagenesis and physical properties. B. Geol. Soc. Denmark. **55**, 97–128 (2007)

Fabricius, I. L., Borre, M. K.: Stylolites, porosity, depositional texture, and silicates in chalk facies sediments. Ontong Java Plateau – Gorm and Tyra fields, North Sea. Sedimentology. **54**, 183–205 (2007). doi:10.1111/j.1365-3091.2006.00828.x

Fabricius, I. L., Hoier, C., Japsen, P., Korsbech, U.: Modelling elastic properties of impure chalk from South Arne field, North Sea. Geophys. Prospect. **55**, 487–506 (2007). doi:10.1111/j.1365-2478.2007.00613.x

Fjær, E., Holt, R. M., Horsrud, P., Raaen, A. M., Risnes, R.: Petroleum related rock mechanics (2nd Edition). Elsevier, Amsterdam, Netherlands. 491–492 (2008)

Frykman, P.: Spatial variability in petrophysical properties in Upper Maastrichtian chalk outcrops at Stevns Klint, Denmark. Mar. Petrol. Geol. **18**, 1041–1062 (2001). doi:10.1016/S0264-8172(01)00043-5

Gaviglio, P., Vandycke, S., Schroeder, C., Coulon, M., Bergerat, F., Dubois, C., Pointeau, I.: Matrix strains along normal fault planes in the Campanian white chalk of Belgium:

structural consequences. Tectonophysics. **309**, 41–56 (1999). doi:10.1016/s0040-1951(99)00131-6

Hart, M. B., Feist, S. E., Price, G. D., Leng, M. J.: Reappraisal of the K–T boundary succession at Stevns Klint, Denmark. J. Geol. Soc. London. **161**, 885–892 (2004). doi:10.1144/0016-764903-071

Hart, M. B., Feist, S. E., Håkansson, E., Heinberg, C., Price, G. D., Leng, M. J., Watkinson, M. P.: The Cretaceous–Palaeogene boundary succession at Stevns Klint, Denmark: Foraminifers and stable isotope stratigraphy. Palaeogeogr. Palaeocl. **224**, 6–26 (2005). doi:10.1016/j.palaeo.2005.03.029

Havmøller, O, Foged, N: Review of rock mechanical data for chalk. Proceedings of 5th North Sea Chalk Sym, Reims (1996).

Hellmann, R., Renders, P., Gratier, J., Guiguet, R.: Experimental pressure solution compaction of chalk in aqueous solutions Part 1. deformation behavior and chemistry. In: Hellmann, R., Wood., S. A. (eds.) Water–Rock Interactions, Ore Deposits, and Environmental Geochemistry: A Tribute to Davod A. Crerar. **7**, 129–152 (2002)

Hermansen, H., Thomas, L. K., Sylte, J. E., Aasboe, B. T.: Twenty five years of Ekofisk reservoir management. In: SPE Annual Technical Conference and Exhibition San Antonio, Texas. 873–885 (1997). doi:10.2118/38927-ms

Hermansen, H., Landa, G. H., Sylte, J. E., Thomas, L. K.: Experiences after 10 years of waterflooding the Ekofisk Field, Norway. J. Petrol. Sci. Eng. **26**, 11–18 (2000). doi:10.1016/s0920-4105(00)00016-4

Hiorth, A., Jettestuen, E., Cathles, L. M., Madland, M. V.: Precipitation, dissolution, and ion exchange processes coupled with a lattice Boltzmann advection diffusion solver. Geochim. Cosmochim. Ac. **104**, 99–110 (2013). doi:10.1016/j.gca.2012.11.019

Hjuler, M. L.: Diagenesis of upper cretaceous onshore and offshore chalk from the North Sea area. PhD thesis, Technical University of Denmark. 11–23 (1997)

Hjuler, M. L., Fabricius, I. L.: Engineering properties of chalk related to diagenetic variations of Upper Cretaceous onshore and offshore chalk in the North Sea area. J. Petrol. Sci. Eng. **68**, 151–170 (2009). doi:10.1016/j.petrol.2009.06.005

Jarvis, I.: The Santonian–Campanian phosphatic chalks of England and France. P. Geologist. Assoc. **117**, 219–237 (2006). doi:10.1016/S0016-7878(06)80011-8

Korsnes, R. I., Strand, S., Hoff, Ø., Pedersen, T., Madland, M. V., Austad, T.: Does the chemical interaction between seawater and chalk affect the mechanical properties of chalk? In:

the International Symposium of the International Society for Rock Mechanics (2006a). doi:10.1201/9781439833469.ch61

Korsnes, R. I., Madland, M. V., Austad, T.: Impact of brine composition on the mechanical strength of chalk at high temperature. In: the International Symposium of the International Society for Rock Mechanics. Liége, Belgium (2006b). doi: 10.1201/9781439833469.ch18

Madland, M. V., Hiorth, A., Omdal, E., Megawati, M., Hildebrand–Habel, T., Korsnes, R. I., Evje, S., Cathles, L. M.: Chemical alterations induced by rock–fluid interactions when injecting brines in high porosity chalks. Transport. Porous Med. **87**, 679–702 (2011). doi:10.1007/s11242-010-9708-3

McLennan, S. M., Taylor, S. R., Hemming, S. R.: Composition, differentiation, and evolution of continental crust: constraints from sedimentary rocks and heat flow. In: Brown, M. & Rushmer, T. (eds.). Evolution and Differentiation of the Continental Crust. Cambridge Univ. Press, 92–134 (2006).

Megawati, M., Andersen, P. Ø., Korsnes, R. I., Evje, S., Hiorth, A., Madland, M. V.: The effect of aqueous chemistry pH on the time–dependent deformation bahavoir of chalk experimental and modelling study. In: Pore2Fluid International Conference. Paris, France (2011)

Megawati, M., Hiorth, A., Madland, M.V.: The impact of surface charge on the mechanical behavior of high–porosity chalk. Rock. Mech. Rock. Eng. **46**, 1073–1090 (2013). doi:10.1007/s00603-012-0317-z

Megawati, M., Madland, M. V., Hiorth, A.: Mechanical and physical behavior of high–porosity chalks exposed to chemical perturbation. J. Petrol. Sci. Eng. **133**, 313–327 (2015). doi:10.1016/j.petrol.2015.06.026

Minde, M. W., Zimmermann, U., Madland, M. V., Korsnes, R. I., Schulz, B., Audinot, J.: Fluid–flow during EOR experiments in chalk: insights using SEM–MLA, EMPA and Nanosims Applications. In: International Symposium of the Society of Core Analysts. Colorado, USA, 21–26 August (2016)

Molenaar, N., Zijlstra, J. J. P.: Differential early diagenetic low–Mg calcite cementation and rhythmic hardground development in Campanian–Maastrichtian chalk. Sediment. Geol. **109**, 261–281 (1997). doi:10.1016/S0037-0738(96)00064-4

Nagel, N. B.: Compaction and subsidence issues within the petroleum industry: From Wilmington to Ekofisk and beyond. Phys. Chem. Earth. Pt. A. **26**, 3–14 (2001). doi:10.1016/S1464-1895(01)00015-1

Nermoen, A., Korsnes, R. I., Hiorth, A., Madland, M. V.: Porosity and permeability development in compacting chalks during flooding of nonequilibrium brines: Insights from long–term experiment. J. Geophys. Res–Sol. Ea. **120**, 2935–2960 (2015). doi:10.1002/2014JB011631

Nermoen, A., Korsnes R. I., Aursjø, O., Madland, M. V., Kjørslevik T. A. C. and Østensen, G.: How Stress and Temperature Conditions Affect Rock-Fluid Chemistry and Mechanical Deformation. Frontiers in Physics. 4, 1-19 (2016). doi: 10.3389/fphy.2016.00002

Neveux, L., Grgic, D., Carpentier, C., Pironon, J., Truche, L., Girard, J. P.: Experimental Simulation of Chemomechanical Processes during Deep Burial Diagenesis of Carbonate Rocks. J. Geophys. Res–Sol. Ea. **119**, 984–1007 (2014). doi: 10.1002/2013JB010516.

Newman, G. H.: The effect of water chemistry on the laboratory compression and permeability characteristics of some North Sea chalks. J. Petrol. Technol. **35**, 976–980 (1983). doi:10.2118/10203-pa

Palandri, J. L., Kharaka, Y. K.: A compilation of rate parameters of water–mineral interaction kinetics for application to geochemical modeling. U. S. Geological Survey. Menlo Park, Ca (2004)

Parkhurst, D. L., Appelo, C. A. J.: Description of input and examples for PHREEQC version 3—a computer program for speciation, batch–reaction, one–dimensional transport, and inverse geochemical calculations. U. S. Geological Survey Techniques and Methods. chap. A43 (2013)

Paterson, M. S. Nonhydrostatic thermodynamics and its geologic applications, Rev. Geophys. Space Phys. **11**, 355–389 (1973). doi:10.1029/RG011i002p00355.

Putnis, A.: Mineral replacement reactions: from macroscopic observations to microscopic mechanisms. Mineral. Mag. **66**, 689–708 (2002). doi:10.1180/0026461026650056

Risnes, R., Flaageng, O.: Mechanical properties of chalk with emphasis on chalk–fluid interactions and micromechanical aspects. Oil. Gas. Sci. Technol. **54**, 751–758 (1999). doi:10.2516/Ogst:1999063

Risnes, R., Madland, M. V., Hole, M., Kwabiah, N. K.: Water weakening of chalk – mechanical effects of water–glycol mixtures. J. Petrol. Sci. Eng. **48**, 21–36 (2005). doi:10.1016/j.petrol.2005.04.004

Ruiz–Agudo, E., Putnis, C. V., Putnis, A.: Coupled dissolution and precipitation at mineral–fluid interfaces. Chem. Geol. **383**, 132–146 (2014). doi:10.1016/j.chemgeo.2014.06.007

Rutter, E. H. The kinetics of rock deformation by pressure solution, Philos. Trans. R. Soc. Lond. **283**, 203–219 (1976).

Schroeder, C., Gaviglio, P., Bergerat, F., Vandycke, S., Coulon, M.: Faults and matrix deformations in chalk: contribution of porosity and sonic wave velocity measurements. B. Acad. Vet. France. **177**, 203–213 (2006). doi:10.2113/gssgfbull.177.4.203

Strand, S., Standnes, D. C., Austad, T.: Spontaneous imbibition of aqueous surfactant solutions into neutral to oil–wet carbonate cores: effects of brine salinity and composition. Energ. Fuel. **17**, 1133–1144 (2003). doi:10.1021/ef030051s

Strand, S., Hjuler, M. L., Torsvik, R., Pedersen, J., Madland, M. V., Austad, T.: Wettability of chalk: impact of silica, clay content and mechanical properties. Petrol. Geosci. **13**, 69–80 (2007). doi:10.1144/1354-079305-696

Surlyk, F., Stemmerik, L., Ahlborn, M., Harlou, R., Lauridsen, B.W., Rasmussen, S.L., Schovsbo, N., Sheldon, E., Thibault, N.: The cyclic Rørdal member – a new lithostratigraphic unit of chronostratigraphic and palaeoclimatic importance in the upper Maastrichtian of Denmark. B. Geol. Soc. Denmark. **58**, 89–98 (2010)

Tang, G.Q., Firoozabadi, A.: Effect of pressure gradient and initial water saturation on water injection in water–wet and mixed–wet fractured porous media. SPE Res. Eval. & Eng. **4**, 516–524 (2001). doi:10.2118/74711-Pa

Van den Bark.,Thomas, O. D.: Ekofisk–1st of the giant oil–fields in Western Europe. AAPG. Bull. **65**, 2341–2363 (1981)

Wang, W., Madland, M. V., Zimmermann, U., Nermoen, A., Korsnes, R. I., Bertolino, S. A. R., Hildebrand–Habel, T.: Evaluation of porosity change during chemo–mechanical compaction in flooding experiments on Liège outcrop chalk. In: Armitage, P. J., Butcher, A. R., Churchill, J. M., Csoma, A. E., Hollis, C., Lander, R. H., Omma, J. E. & Worden, R. H. (eds) Reservoir Quality of Clastic and Carbonate Rocks: Analysis, Modelling and Prediction. J. Geol. Soc. London. Special Publications, **435**. doi:10.1144/SP435.10

Wright, E. K.: Stratification and paleocirculation of the late Cretaceous Western interior seaway of North America. Geol. Soc. Am. Bull. **99**, 480–490 (1987)

Yasuhara, H., Elsworth, D., Polak, A. A mechanistic model for compaction of granular aggregates moderated by pressure solution. Journal of Geophysical Research-Solid Earth. 2003.108, doi: 10.1029/2003JB002536

Zhang, P., Austad, T.: Wettability and oil recovery from carbonates: effects of temperature and potential determining ions. Colloid. Surface. A. **279**, 179–187 (2006). doi:10.1016/j.colsurfa.2006.01.009

Zhang, X., Spiers, C. J., Peach, C. J.: Compaction creep of wet granular calcite by pressure solution at 28 °C to 150 °C. J. Geophys. Res. **115**, 1–18 (2010). doi:10.1029/2008jb005853

Zhang, X., Spiers, C. J., Peach, C. J.: Effects of pore fluid flow and chemistry on compaction creep of calcite by pressure solution at 150 °C. Geofluids. **11**, 108–122 (2011). doi:10.1111/j.1468-8123.2010.00323.x

Zimmermann, U., Madland, M. V., Bertolino, S. A. R., Hildebrand–Habel, T.: Tracing fluid flow in flooded chalk under long term test conditions. In: 75th EAGE Conference & Exhibition incorporating SPE. London (2013)

Zimmermann, U., Madland, M. V., Nermoen, A., Hildebrand–Habel, T., Bertolino, S. A. R., Hiorth, A., Korsnes, R. I., Audinot, J. N., Grysan, P.: Evaluation of the compositional changes during flooding of reactive fluids using scanning electron microscopy, nano–secondary ion mass spectrometry, X–ray diffraction and whole rock geochemistry. AAPG. Bull. **99**, 791–805 (2015). doi:10.1306/12221412196